Astronomy
&
Astrophysics

Coalescing neutron stars – A step towards physical models

III. Improved numerics and different neutron star masses and spins

M. Ruffert[1] and H.-Th. Janka[2]

[1] Department of Mathematics & Statistics, University of Edinburgh, Edinburgh, EH9 3JZ, Scotland, UK
[2] Max-Planck-Institut für Astrophysik, Postfach 1317, 85741 Garching, Germany
  e-mail: thj@mpa-garching.mpg.de

Abstract. In this paper we present a compilation of results from our most advanced neutron star merger simulations. Special aspects of these models were refered to in earlier publications (Ruffert & Janka 1999; Janka et al. 1999), but a description of the employed numerical procedures and a more complete overview over a large number of computed models are given here. The three-dimensional hydrodynamic simulations were done with a code based on the Piecewise Parabolic Method (PPM), which solves the discretized conservation laws for mass, momentum, energy and, in addition, for the electron lepton number in an Eulerian frame of reference. Up to five levels of nested cartesian grids ensure higher numerical resolution (about $0.6\,\mathrm{km}$) around the center of mass while the evolution is followed in a large computational volume (side length between 300 and $400\,\mathrm{km}$). The simulations are basically Newtonian, but gravitational-wave emission and the corresponding back-reaction on the hydrodynamic flow are taken into account. The use of a physical nuclear equation of state allows us to follow the thermodynamic history of the stellar medium and to compute the energy and lepton number loss due to the emission of neutrinos. The computed models differ concerning the neutron star masses and mass ratios, the neutron star spins, the numerical resolution expressed by the cell size of the finest grid and the number of grid levels, and the calculation of the temperature from the solution of the entropy equation instead of the energy equation. The models were evaluated for the corresponding gravitational-wave and neutrino emission and the mass loss which occurs during the dynamical phase of the merging. The results can serve for comparison with smoothed particle hydrodynamics (SPH) simulations. In addition, they define a reference point for future models with a better treatment of general relativity and with improvements of the complex input physics. Our simulations show that the details of the gravitational-wave emission are still sensitive to the numerical resolution, even in our highest-quality calculations. The amount of mass which can be ejected from neutron star mergers depends strongly on the angular momentum of the system. Our results do not support the initial conditions of temperature and proton-to-nucleon ratio needed according to recent work for producing a solar r-process pattern for nuclei around and above the $A \approx 130$ peak. The improved models confirm our previous conclusion that gamma-ray bursts are not powered by neutrino emission during the dynamical phase of the merging of two neutron stars.

Key words. stars: neutron – binaries: close – hydrodynamics – gravitational waves – nuclear reactions, nucleosynthesis, abundances – elementary particles

1. Introduction

The binary pulsar PSR 1913+16 (Hulse & Taylor 1975) is the most famous example for a binary system containing two neutron stars, among another $\sim$1000 of such systems expected to exist in our Galaxy. High-precision measurements show that the change in time of the orbital parameters of PSR 1913+16 is consistent with expectations from the theory of general relativity, which predicts the

emission of gravitational waves and a continuous decrease of the orbital separation. Therefore, these systems have a finite lifetime of typically hundreds of millions up to billions of years. As the two stars spiral in towards each other, the evolution accelerates because the gravitational-wave emission rises strongly with decreasing distance. When the orbital separation has shrunk to only a few stellar radii, the system has become a strong source of gravitational waves with a frequency around $100\,\mathrm{Hz}$. It will end its life within milliseconds in the final, catastrophic merging of the two neutron stars, emitting a powerful outburst of

---

gravitational radiation which carries important information about the properties of the merging stars, the dynamics of the coalescence, and the remnant left behind.

With an estimated rate of about 10^{-5} events per year per galaxy (e.g., see the recent numbers in Bulik et al. 1999; Fryer et al. 1999; Kalogera & Lorimer 2000, and references therein) neutron star mergers are among the most frequent and most promising candidates for gravitational-wave emission which is strong enough to be measurable by the upcoming interferometric experiments in the US (LIGO), Europe (GEO600, VIRGO), and Japan (TAMA) (Thorne 1995). Theoretical models and wave templates, however, are needed to help filter out the weak signals from disturbing background noise. Gravitational waves from neutron star mergers could be one of the most fruitful ways to learn about the internal properties of neutron stars.

Merging neutron stars are also considered as possible sources of at least the subclass of short and hard cosmic gamma-ray bursts, especially if the merger remnant collapses to a black hole on a dynamical timescale (for recent discussions and model calculations, see, e.g., Popham et al. 1999; Ruffert & Janka 1999). Coincident detections of gravitational waves and gamma rays would be a convincing observational confirmation of this hypothesis and might in fact be the only possibility to identify the central engine of a gamma-ray burst unequivocally. The X-ray satellite HETE-2, which was launched in Fall 2000, is hoped to bring a similar breakthrough in the observation of short bursts as the BeppoSAX satellite did in case of the long ones.

The energy of the relativistically expanding fireball or jet, which finally produces the observable gamma-ray burst, can be provided by the annihilation of neutrino-antineutrino pairs (Paczyński 1991; Mészáros & Rees 1992; Woosley 1993a) or possibly by magnetohydrodynamical processes (Blandford & Znajek 1977; Mészáros & Rees 1997). In the former case, the gravitational binding energy of accreted disk matter is tapped, in the latter case the rotational energy of the central black hole could be converted into kinetic energy of the outflow. If neutrino processes are supposed to power the gamma-ray burst phenomenon, very high neutrino luminosities are needed, of magnitude similar as those from core-collapse supernovae. The rate of neutron star mergers, however, is much smaller (by a factor of 100–10 000) than the Galactic supernova rate. This practically excludes them as detectable sources of thermal neutrinos in the MeV energy range, because the signals are too faint to be measurable from extragalactic distances. Dissipative processes in the relativistic outflow, which are considered to produce the gamma-ray burst, may also lead to the generation of high-energy or even ultra high-energy neutrinos (Paczyński & Xu 1994; Waxman & Bahcall 1997, 2000). Such neutrinos might be seen in future km^2-scale experiments like ICECUBE, which is currently under construction in the Antarctica. However, they do not carry much specific information about the origin of the relativistically moving particles and it is therefore not

very likely that they can yield much evidence about the nature of the central engine that powers the gamma-ray burst.

Neutron-rich matter, which is ejected from the system during the dynamical phase of the merging, was suggested as a possible site for the rapid neutron capture process (r-process) to produce heavy nuclei beyond the iron group (Lattimer et al. 1974, 1976; Hilf et al. 1974; Eichler et al. 1989; Meyer 1989). This problem has gained new interest recently (Rosswog et al. 1999, 2000; Freiburghaus et al. 2000). The possible contribution to the Galactic r-process material is estimated from the gas mass that gets unbound during the violent last stages of the coalescence. The nuclear reactions in decompressed neutron star matter depend sensitively on the initial conditions (neutron excess, composition, temperature, density), the dynamical and, in particular, thermal history of the material, and the influence of beta-decays and corresponding neutrino losses. All of these issues are so far not well under control in theoretical models, and therefore hydrodynamic simulations of neutron star mergers have not (yet?) been able to yield conclusive results.

These questions have been the motivation for a large number of investigations of the spiral-in phase and the ultimate merging of neutron stars. Analytic studies and ellipsoidal treatments concentrated on the effects of viscous dissipation for the heating and the rotation of the stars (Kochanek 1992; Bildsten & Cutler 1992; Lai 1994), the final instability of the mass transfer near the tidal radius (e.g., Bildsten & Cutler 1992; Lai et al. 1994a,b; Taniguchi & Nakamura 1996; Lai & Wiseman 1996; Lombardi et al. 1997; Baumgarte 2001) and the deformed equilibrium structure and tidal lag of the binary configuration prior to the dynamical interaction (Lai & Shapiro 1995). Hydrodynamical simulations of the coalescence were performed for Newtonian gravity with SPH codes (e.g., Rasio & Shapiro 1992, 1994, 1995; Centrella & McMillan 1993; Zhuge et al. 1994, 1996; Davies et al. 1994; Rosswog et al. 1999, 2000) and with grid-based methods (e.g., Oohara & Nakamura 1990; Nakamura & Oohara 1991), partly including special treatments of the gravitational-wave emission and their back-reaction on the flow by adding the corresponding post-Newtonian terms to the equations of hydrodynamics (e.g., Ruffert et al. 1996, 1997a; Ruffert et al. 1997b). More recently progress has been achieved in a wider use of the post-Newtonian approximation (Shibata et al. 1998; Ayal et al. 2001; Faber & Rasio 2000; Faber et al. 2001) and considerable advances were made towards general relativistic treatments (Oohara & Nakamura 1999; Shibata 1999; Shibata & Uryū 2000, 2001).

A spectacular result was obtained by Mathews & Wilson (1997, and references therein) who found that relativistic effects lead to a compression of the two neutron stars during the late stages of the spiral-in and therefore to their gravitational collapse to black holes prior to the merging. This effect contradicts Newtonian models where tidal stretching reduces the density of the stars as they get closer. Analytic considerations confirm the Newtonian

behavior also for the post-Newtonian case (Thorne 1998; Baumgarte et al. 2000,b), and more recent simulations by the Wilson group (Marronetti et al. 1999) as well as general relativistic hydrodynamic models by other groups (Bonazzola et al. 1999; Shibata et al. 1998) were not able to reproduce the result of Mathews & Wilson (1997). The latter was recognized to be due to an error in the approximation scheme to full general relativity (Flanagan 1999). In any case, pre-merging collapse of the neutron stars is a speculative option only if the nuclear equation of state is extraordinarily soft and the neutron stars are already very close to the maximum mass for stable single neutron stars.

The majority of the simulations by other groups was done with simple microphysics, in particular with a polytropic law $P = K\rho^{\Gamma}$ for the equation of state (EoS) of the neutron star matter. This is a fair approach when one is mainly interested in the calculation of the gravitational-wave emission, which is associated with the motion of the bulk of the mass. It offers the advantage that the influence of the stiffness of the EoS, which determines the mass-radius relation of the neutron stars and the amount of compression which occurs during the final plunge, can be easily studied by choosing different values for the adiabatic index Γ.

Several years ago we started to compute merger models with a more elaborate treatment of the EoS of the neutron star matter, using the physical description by Lattimer & Swesty (1991), which enabled us to follow the thermodynamics of the gas and to include a treatment of the neutrino production and emission from the heated neutron stars (Ruffert et al. 1996, 1997a; Ruffert & Janka 1998, 1999; Janka et al. 1999). Our main aims were the investigation of the relevance for gamma-ray burst scenarios, in particular for those where the neutrino emission had been suggested to provide the energy for the relativistic gamma-ray burst fireball via neutrino-antineutrino annihilation. Also the amount of mass ejection during the dynamical interaction and the properties of the ejected matter depend on the EoS, which cannot be descibed by one simple polytropic law in both the low-density and high-density regimes.

After publication of our first papers (Ruffert et al. 1996, 1997a), we changed our code considerably and, in particular, we improved many features which had influence on the results of our simulations. For example, we introduced nested grids to get a higher resolution of the neutron stars and at the same time to use a larger computational volume. In addition, we extended the EoS table to higher temperatures and lower densities. The latter allowed us to reduce the density of the dilute medium that has to be assumed around the neutron stars on the Eulerian grid. Since the heat capacity of cold, degenerate matter is very small, minor numerical noise in the internal energy had induced larger errors in the temperature. We therefore also implemented an entropy equation, because the entropy is numerically less problematic for calculating the temperature. Besides these improvements, we also

covered a wider range of scenarios, e.g., added models with opposite directions of the neutron star spins and with different neutron star masses as well as different mass ratios.

All of our later publications referred to data of models which were computed with the improved version of the code. So did the simulations of the black hole accretion in Ruffert & Janka (1999) start from an initial model of the new generation of calculations, and also in the tables of Janka et al. (1999) data of new neutron star merger models were listed. So far, however, we published only very specific aspects of these new models and did not present our results in detail. This is the purpose of the present publication.

In Sect. 2 we will give a technical description of the code changes and improvements, in Sect. 3 a list of computed models, in Sect. 4 we shall present the main results for the new models, and in Sect. 5 we shall discuss the implications and draw conclusions.

2. Changes and improvements of the numerics

The three-dimensional Eulerian hydrodynamical conservation laws for mass, momentum and energy for non-viscous flow are integrated explicitly in time on a cartesian grid, using a finite-volume scheme which is based on the Piecewise Parabolic Method (PPM) of Colella & Woodward (1984). The code is basically Newtonian, but includes the post-Newtonian terms that account for the local effects of gravitational-wave emission (the volume integral of these local terms reproduces the quadrupole approximation) and the corresponding back-reaction on the hydrodynamical flow according to the formulation by Blanchet et al. (1990) (for details, see Ruffert et al. 1996). The Poisson equations for the gravitational potential and two additional potentials used in the back-reaction terms are solved by fast Fourier transforms. For the described neutron star merger simulations, the thermodynamics of the stellar medium are described by a tabular version of the Lattimer & Swesty (1991) EoS, which allows us to take into account the source terms for energy and lepton number loss due to neutrino production. These source terms are calculated with a neutrino trapping scheme which evaluates the production rates of neutrinos and antineutrinos of all flavors. The trapping scheme takes into account the optical depth at any location inside the star to reduce the neutrino release when the diffusion timescale becomes long. Since the emission of electron neutrinos and antineutrinos can change the electron lepton number of the stellar medium, we also solve a continuity equation for this quantity. A detailed discussion of the equations and a more complete explanation of the numerical methods can be found in Ruffert et al. (1996, 1997a).

The numerical code and the input physics described in Ruffert et al. (1996, 1997a) have been changed and improved in a number of aspects.

(i) Grid:
The cartesian grid for the simulations presented there had a side length of only 82 km. Therefore a significant amount
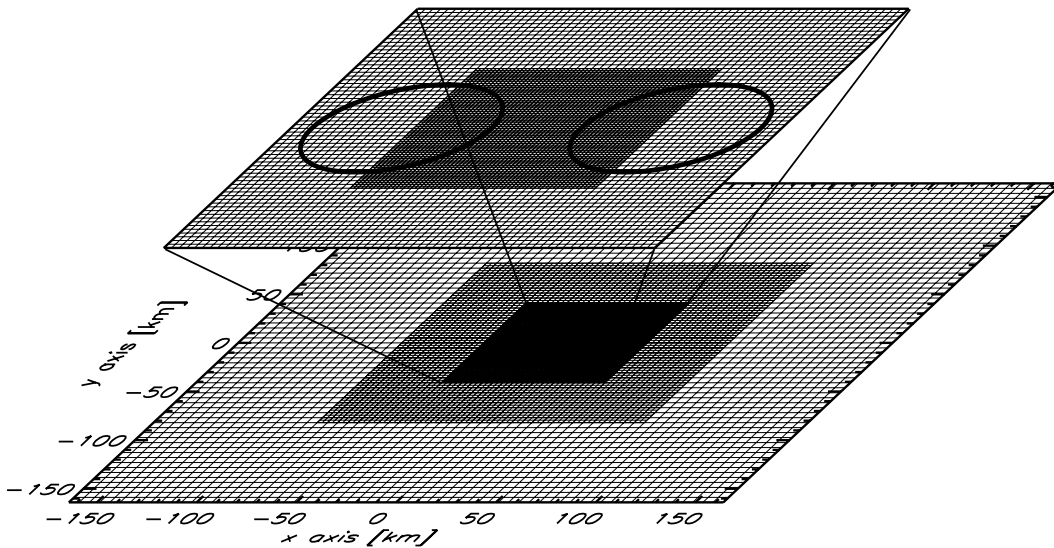
Fig. 1. Illustration of four levels of nested grids in two (instead of three) spatial dimensions, each level with 64 cells in every direction, covering a computational volume with side length of 328 km. The innermost two grid levels are enlarged and the initial positions of the two neutron stars in the orbital plane are indicated.

of mass was swept off the grid although it would not have become unbound. For this reason we enlarged the computational volume to 328–656 km by introducing up to five levels of nested grids (Fig. 1). This ensures good numerical resolution near the grid center so that the two neutron stars are represented in the new calculations with a similar accuracy as the best resolved Model A128 in Ruffert et al. (1996, 1997a). The larger computational volume allows us to trace the matter with high angular momentum, which is flung out to large distances but returns and is added to the cloud of gas that surrounds the compact merger remnant.

(ii) EoS table:
Another problem in the previous calculations was that under certain extreme conditions (e.g., extreme heating as in case of Model C64) the boundaries of the EoS table were hit. Therefore we expanded the temperature range in a new EoS table to cover values from 10^{-2} MeV to 100 MeV, and reduced the minimum density to $5 \times 10^7 \, \mathrm{g \, cm^{-3}}$.

(iii) Environmental density:
Since the simulations are done in an Eulerian reference frame, the density outside the neutron stars cannot be set to zero but only to a small value, i.e., a value small compared to the average density in the stellar interior. In order not to influence the dynamical behavior of the ejected stellar fragments by gas that is swept up in the surroundings, the density of this ambient medium should be chosen as low as possible. Therefore we used a value of $10^8 \, \mathrm{g \, cm^{-3}}$ in the new calculations instead of $10^9 \, \mathrm{g \, cm^{-3}}$ previously. The total mass of this dilute gas on the grid is therefore significantly less than $10^{-3} \, M_\odot$. Since only an extremely small fraction of this gas interacts with the neutron star matter, the dynamical effect of this medium is negligible.

(iv) Temperature determination and entropy equation:
The employed hydrodynamics code solves the energy equation for the total specific energy, which is the sum of the specific internal and kinetic energies. Compared to integrating an equation for the internal energy alone, this has the advantage that without gravity the energy equation is written in a fully conservative way. The effects of gravity are included by source terms. It has, however, the disadvantage that the internal energy, from which the temperature is determined, has to be calculated as the difference of total and kinetic energies. If both the latter energies are large, a small value of the internal energy can be significantly affected by numerical noise, and the temperature determination can become inaccurate. This is usually not a problem, but does become problematic in the case of extremely degenerate neutron star matter, which has a very small heat capacity. Only minor variations of the internal energy can then lead to much larger changes of the temperature. For these reasons the temperature is a quantity which is very sensitive to numerical deficiencies. As a consequence, it was not possible to start the simulations in Ruffert et al. (1996, 1997a) with cold neutron stars. A stable temperature evolution could be obtained when the thermal energy density in the initial configuration was assumed to be two per cent of the degeneracy energy density. With this prescription, the central temperature of the neutron stars was several MeV and the surface temperature about half an MeV initially. Nevertheless, the corresponding neutrino luminosities were negligibly small, and the total thermal energy was so tiny compared to the other energies (internal, gravitational and kinetic) that its effect on the dynamics was unimportant.

In order to avoid these problems in the temperature determination and to have the freedom of starting with colder neutron stars, we decided to use the entropy instead of the energy density for temperature calculations. The entropy evolution was followed by a separate entropy equation which was integrated in addition to the hydrodynamic conservation laws. In an Eulerian frame of

reference, the corresponding continuity equation is (making use of Einstein's summation convention)

$$\frac{\partial}{\partial t}(s\,n_\mathrm{b}) + \frac{\partial(s\,n_\mathrm{b}v^j)}{\partial x^j} = S_\nu + S_\mathrm{sh} + S_\mathrm{vis}\,. \tag{1}$$

Here s means the matter entropy per nucleon, $n_\mathrm{b} = \rho/u$ the baryon number density (u being the atomic mass unit, ρ the rest mass density), and v^j the cartesian components of the velocity vector. The divergence of the entropy flux was written in its cartesian form (summation is applied when an index appears twice), and the source terms on the right hand side are the rates of change of the entropy density due to neutrino production, shock dissipation, and shear and bulk viscosity effects, respectively.

The entropy generation rate per unit volume by neutrino processes is (e.g., Cooperstein 1988)

$$S_\nu = \frac{S_\mathrm{E}}{k_\mathrm{B}T} - S_\mathrm{L}\left(\psi_\mathrm{e} + \psi_\mathrm{p} - \psi_\mathrm{n}\right)\,, \tag{2}$$

where S_E and S_L are the effective energy loss rate and the effective lepton number source term as defined in Appendix B of Ruffert et al. (1996), $k_\mathrm{B}T$ is the temperature in MeV and the ψ's denote the degeneracy parameters (chemical potentials divided by the temperature) of electrons, protons and neutrons (including the rest mass energies). The neutrino source terms as given by Ruffert et al. (1996) are only evaluated for temperatures above about 0.5 MeV. Below this threshold they are switched off, because the assumptions employed in their calculation are not valid any more.

The entropy generation rate per unit volume by shocks is given according to the tensor formalism of Tscharnuter & Winkler (1979) as

$$S_\mathrm{sh} = -\frac{Q_k^i\epsilon_i^k}{k_\mathrm{B}T}\,, \tag{3}$$

with the mixed tensor Q_l^m of the viscous pressure given by

$$Q_l^\mathrm{m} = \begin{cases} l^2\rho\,\dfrac{\partial v^k}{\partial x^k}\left(\epsilon_l^\mathrm{m} - \dfrac{\delta_l^\mathrm{m}}{3}\dfrac{\partial v^k}{\partial x^k}\right), & \text{if } \dfrac{\partial v^k}{\partial x^k} < 0; \\[2ex] 0, & \text{otherwise,} \end{cases} \tag{4}$$

and the mixed tensor ϵ_l^m of the symmetrized gradient of the velocity field defined by

$$\epsilon_l^\mathrm{m} = \frac{1}{2}\left(\frac{\partial v^\mathrm{m}}{\partial x_l} + \frac{\partial v_l}{\partial x^\mathrm{m}}\right)\,, \tag{5}$$

where Einstein's summation convention is used ($\partial v^k/\partial x^k$ therefore means the divergence of the velocity vector in cartesian coordinates), and δ_l^m is the mixed unity tensor. The characteristic length l is of the order of the local width of the grid, $l = f\cdot\Delta x$. We calibrated the proportionality factor f such that the entropy jump across a shock as calculated with our hydrodynamics code is reproduced by the entropy generation according to Eqs. (3)–(5). We found best agreement for the choice of $f = 1.8$.

The entropy generation rate per unit volume due to shear and bulk viscosity can be written (using again the summation convention) as (e.g., Shapiro & Teukolsky 1983; Landau & Lifschitz 1991)

$$S_\mathrm{vis} = \frac{1}{k_\mathrm{B}T}\left[\frac{1}{2}\,\eta\left(\frac{\partial v^i}{\partial x^j} + \frac{\partial v^j}{\partial x^i}\right)^2 - \frac{2}{3}\,\eta\left(\frac{\partial v^k}{\partial x^k}\right)^2 \right.$$
$$\left. + \zeta\left(\frac{\partial v^k}{\partial x^k}\right)^2\right]\,, \tag{6}$$

where η is the dynamic shear viscosity coefficient and ζ the bulk viscosity coefficient. Solving the Euler equations for an ideal fluid, shear viscosity effects are only caused by the numerical viscosity of our hydrodynamics code, which we describe by the ansatz $\eta = \alpha\rho v\Delta x$. With a typical grid resolution Δx between 10^4 cm and 10^5 cm one empirically finds values for α between 5×10^{-4} and 5×10^{-3} (Janka et al. 1999). We used a representative number of $\alpha = 2\times 10^{-3}$ in the simulations discussed below.

In hot neutron star matter with the proton fraction exceeding a critical lower limit, bulk viscosity can be strongly enhanced by the direct URCA processes of electron neutrino and antineutrino production and absorption (Haensel & Schaeffer 1992). For matter composed of neutrons (n), protons (p) and electrons (e) with trapped neutrinos (but with no trapped lepton-number excess, i.e., if $\psi_\mathrm{e} + \psi_\mathrm{p} - \psi_\mathrm{n} \ll 1$) one can write an approximate expression for the bulk viscosity coefficient as $\zeta \sim 10^{24}(Y_\mathrm{p}\rho/\rho_0)^{1/3}$ g/(cm s) with $Y_\mathrm{p} = Y_\mathrm{e}$ being the proton fraction and $\rho_0 \approx 2.5\times 10^{14}$ g/cm^3 the density of normal nuclear matter (Haensel & Schaeffer 1992; Sawyer 1980; van den Horn & van Weert 1981). Although the numerical factor was taken somewhat larger than estimated by Haensel & Schaeffer (1992), we found the entropy generation rate associated with the bulk viscosity term to be negligibly small.

The entropy loss rate due to neutrino emission, expressed by the source term S_ν, is tiny initially, but becomes (globally, i.e. as an integral over all grid cells) comparable to the (positive) shear viscosity term S_vis after several milliseconds, when the neutron stars have merged to a hot, rapidly and differentially spinning object. Earlier than this, in particular prior to the merging, the time is too short for shear viscosity to raise the entropy, and the temperature is too low for neutrinos to make any effect. When the neutron stars begin to touch (roughly half a millisecond after the simulations were started), the shock dissipation term S_sh becomes clearly the dominant one globally, about twice to twenty times bigger than S_vis.

Using Eq. (1) for evolving the entropy, an updated value of the temperature is obtained in a predictor-corrector step which ensures second order accuracy for the time integration. In a first step one evaluates the entropy source terms with the old temperature, then solves Eq. (1) to get an estimate for the new entropy and thus for the new temperature, and then solves Eq. (1) a second time with source terms computed with an average value of the old and estimated new temperature.

The temperature thus obtained from the entropy equation is used to calculate the neutrino source terms in the hydrodynamic conservation laws of mass, momentum, energy, and lepton number, which still describe the evolution of the stellar fluid. This is not fully consistent and should therefore not be considered as the necessarily better treatment. Instead, it is meant as an alternative approach which allows one to test the uncertainties associated with the temperature determination and the corresponding effects of neutrinos.

(v) Neutrino treatment:
Let us conclude this section with a few remarks about the treatment of neutrinos. The energy radiated in neutrinos during the computed evolution (about 10 ms) is typically more than an order of magnitude smaller than the total energy emitted in gravitational waves. Whereas neutrino emission is very small during the first five milliseconds, it increases later and dominates the energy loss in the second half of the computed evolution. For the dynamical phase of the merging process (which lasts only a few milliseconds after the start of the simulations), neutrino source terms are therefore insignificant. Of course, the treatment of neutrino effects by using a trapping scheme (Ruffert et al. 1996, 1997a) is a strong simplification of the true problem. An exact treatment would require three-dimensional, time-dependent (general relativistic) transport of neutrinos and antineutrinos in a moving neutron star medium, which is extremely optically thick in dense and hot regions and transparent near the stellar surface and in regions where the matter is cold with temperatures below about 1 MeV. Solving this problem is currently not feasible, but we are convinced that our trapping scheme is a good first approach which yields an approximate description of effects connected with the production of neutrinos, and a reasonably good estimate for the total luminosity of neutrinos.

Neutrinos stream off freely as soon as they are produced in transparent matter, thus changing the quantity X_{m} (i.e., energy, entropy or lepton number) of the stellar medium according to the rate given by the neutrino source term S_ν:

$$\frac{\partial X_{\mathrm{m}}}{\partial t} = S_\nu . \qquad (7)$$

In contrast, the dominant mode of energy, entropy and lepton number loss is by neutrino diffusion when neutrinos are in equilibrium with the stellar medium at high optical depths. This is expressed by the equation

$$\frac{\partial (X_{\mathrm{m}} + X_\nu)}{\partial t} = -\nabla F_\nu . \qquad (8)$$

The description used in the trapping scheme is guided by these cases. It calculates the loss terms for energy (and entropy) and lepton number from the local neutrino emission rates in the optically thin regime, and from the rate of diffusive depletion of the equilibrium densities of neutrino number and energy in the optically thick regime. The transition between both limits is done with a smooth interpolation based on the local diffusion timescale, which is estimated from the optical depth to the stellar surface (see Appendix B in Ruffert et al. 1996). In the equilibrium regime, however, we neglect the contributions of neutrinos to the internal energy density and to the entropy density, or, in other words, we neglect that neutrinos in equilibrium contribute to the heat capacity of the stellar matter (an effect which would affect the computed temperature). A similar approximation is also applied for the (electron) lepton number because we solve a continuity equation only for the net electron number density (number density of electrons minus number density of positrons) and neglect the lepton numbers carried by electron neutrinos and antineutrinos. These approximations can be justified by the fact that the chemical potential of the electrons is much larger than that of neutrinos. Therefore the net lepton number of electron neutrinos minus antineutrinos is very small, and the summed energy densities of neutrinos and antineutrinos of all flavors are always less than ∼10% of the energy density of electrons (plus positrons, if present) plus photons, and even smaller compared to the total internal energy density of the gas, which also includes the contributions of nucleons and nuclei. For the same reason, we also made no effort to take into account the neutrino pressure (or momentum transfer to the stellar medium when neutrinos start to decouple).

The use of a trapping scheme means that neutrino diffusion or propagation relative to the stellar medium and neutrino advection along with the fluid motion are ignored. Therefore the corresponding energy and lepton number (and entropy) transport inside the star are disregarded. These effects are likely not to be very important within the few milliseconds of the computed evolution, because the diffusion timescale in the dense, hot interior of neutron stars is several seconds and neutrino lepton number and energy are small compared to the medium quantities. Even in the less dense region between neutrinosphere and nuclear core the changes of energy and lepton number due to local processes (which are evaluated with the trapping scheme) should dominate the transfer of energy and leptons by neutrinos which stream from one region of the star to another. Therefore we think that the trapping scheme is suitable to account for the main effects which play a role on millisecond timescales. If the simulations were continued for a longer time, tens or hundreds of milliseconds, the transport effects would, of course, have to be included.

The trapping scheme fails to yield a suitable approximation when and where neutrino heating is stronger than neutrino cooling. This is the case outside of the neutrinosphere. Here high-energy neutrinos transfer energy to the cooler stellar gas via scattering and absorption reactions. This energy deposition causes an outflow of baryonic mass, the so-called neutrino-driven wind, which has been investigated in some detail for cooling proto-neutron stars in type-II supernovae (Duncan et al. 1986; Woosley 1993b; Qian & Woosley 1996). It is a major disadvantage that the trapping scheme does not allow one to study this

interesting phenomenon in the context of merging neutron stars. We shall try to remove this deficiency in future improvements of our code.

3. New simulations

In this section we shall describe the different models and will review the most important results of our simulations.

Binaries with different baryonic masses of the neutron stars, 1.2, 1.6, and 1.8 $M_\odot$, were considered, with different mass ratios (1:1 and 1:1.5), and with different neutron star spins, where we distinguish the four cases of initially irrotational systems ("none"), synchronous (or "tidally locked") rotation ("solid"), counterrotation ("anti"), and opposite spin directions ("oppo") of the two neutron stars. The angular velocity due to the spins, which is added to the orbital motion, is equal to the angular velocity of the orbit at the chosen initial distance of the two stars, but the spin directions are varied between the four cases (see also Ruffert et al. 1996). In addition, we computed models with different grids, i.e., with different zone sizes of the finest grid (and thus different numerical resolution) as well as different numbers of grid levels. Finally, we used the entropy equation to follow the temperature history of our models, and started the computations with different temperatures of the neutron stars, "warm" models with a central temperature of 5–7 MeV, satisfying the requirement that the thermal energy at the beginning is two per cent of the internal energy, and "cold" models with a constant initial temperature of only 0.05 MeV.

3.1. Initial conditions

The initial configuration consists of two spherically symmetric neutrons stars, constructed as hydrostatic equilibrium solutions for Newtonian gravity and the EoS of Lattimer & Swesty (1991). The temperature of cold and warm models is chosen as mentioned above, and the profile of the electron fraction, $Y_e(r)$, corresponds to the equilibrium state of cold, deleptonized, neutrino-transparent neutron stars (i.e., the chemical potential of electron neutrinos vanishes throughout the star). The 1.6 $M_\odot$ neutron star has a radius of about 15 km, the 1.2 $M_\odot$ star is slightly smaller and the 1.8 $M_\odot$ star a little bigger. This scaling of mass and radius indicates that the effective adiabatic index of the stellar matter is larger than two (see Shapiro & Teukolsky 1983). The initial center-to-center distance a_0 of the two stars was set to a value such that the stars could finish about one full revolution before the final plunge occurred at the radius of tidal instability. Circular orbits were assumed for all models. The initial orbital velocity was chosen according to the inspiraling motion of two point masses M_1 and M_2 at separation a_0 in response to their emission of gravitational waves. From the quadrupole formula the angular velocity and the radial velocity can

be calculated as (Cutler & Flanagan 1994):

$$\omega = \sqrt{\frac{G(M_1 + M_2)}{a_0^3}}, \tag{9}$$

$$v_r = \dot{a} = -\frac{64}{5}\frac{G^3}{c^5}\frac{1}{a_0^3}M_1M_2(M_1 + M_2). \tag{10}$$

More details about the treatment of the initial conditions can be found in Ruffert et al. (1996).

3.2. Models

Table 1 contains a list of computed models with their specific characteristics. Basically we distinguish models of types A, B, C, O, S and D. Models A, B, C and O are our standard cases with two equal neutron stars with baryonic masses of 1.6 $M_\odot$ and initially irrotational (spin: "none"), corotational ("solid"), counterrotational ("anti") and opposite directions ("oppo"), respectively, for the spins in the initial state. The S-models are computed with smaller, 1.2 $M_\odot$ neutron stars, and the D-models with two different neutron stars of 1.2 $M_\odot$ and 1.8 $M_\odot$. (Note that Model V64 in Janka et al. 1999 is identical to Model C64c of this work.)

The names of the models carry information also about the number of zones of each grid level (32, 64, or 128), and about the number of grid levels, indicated by a superscript, if it is not the standard value of 4. Since we take the extension of the grid in the z-direction perpendicular to the orbital plane to be only half as big as in the orbital plane and, in addition, assume equatorial symmetry, the grids have $32 \times 32 \times 8$ or $64 \times 64 \times 16$ or $128 \times 128 \times 32$ zones, respectively. A higher grid level has only half the resolution (twice the zone size) of the level below. With an equatorial length and width of the computational volume between 328 and 656 km, the smallest zones have a side length between 0.32 km and 1.56 km. For fixed computational volume a smaller number of grid levels implies that the individual grids are bigger, and avoids that the two neutron stars cross the boundary of the innermost grid during spiral in, as they do for our standard case of four levels of nested grids (see Fig. 1). Reducing the number of grid levels therefore allows one to test the corresponding numerical effects.

Use of the entropy instead of the energy to calculate the temperature (which is then used for computing the neutrino emission) is indicated by an extension of the model name. The letter "w" marks the "warm" models, "c" the "cold" ones. Since our stars have to be embedded by a medium with finite density on the Eulerian grid, the motion of the stars through this medium creates a shock wave at the stellar surfaces, where the temperature increases in a narrow ring of grid zones. This effect is energetically umimportant, and also does not lead to a significant increase of the neutrino luminosity as long as the volume and the density of the heated medium stay low. However it is unphysical and can lead to an inflation of the surface layers of the neutron stars. Therefore we

Table 1. Computed models with their characterizing parameters and results. The models differ concerning the chosen initial spins of the neutron stars. In several cases the temperature evolution was followed by using an entropy equation, starting from "high" ("ent wa") or low initial temperature ("ent co"). Also a special choice of the grid is indicated by the model name and in the column with remarks. N is the number of grid zones per dimension in the orbital plane, g the number of levels of the nested grid, L the size of the largest grid, l the size of the smallest zone, M_1 and M_2 are the masses of the two neutron stars, a_0 is their initial center-to-center distance, $k_B T_0$ the initial maximum temperature (reached at the center of the neutron stars), t_{sim} the computed period of time of the evolution, $M_{\rho<11}$ is the gas mass with a density below 10^{11} g/cm^3 at the end of the simulation, M_d the gas mass with specific angular momentum larger than the Keplerian angular momentum at a radius equal to three Schwarzschild radii of the merger remnant, M_g the mass of the gas which leaves the grid, M_u the gas mass which can become unbound, and $k_B T_{mx}$ the maximum temperature reached on the grid during the simulation. The > signs indicate that the numbers are still changing when the simulations were stopped.

model	remark	spin	N	g	L km	l km	M_1 $M_\odot$	M_2 $M_\odot$	a_0 km	$k_B T_0$ MeV	t_{sim} ms	$M_{\rho<11}$ $M_\odot/100$	M_d $M_\odot/100$	M_g $M_\odot/100$	M_u $M_\odot/100$	$k_B T_{mx}$ MeV
A32	—	none	32	4	328	1.28	1.6	1.6	42.	5.44	10.	4.5	6.1	0.78	0.03	53.
A64	—	none	64	4	328	0.64	1.6	1.6	42.	5.47	10.	5.8	8.0	1.78	0.23	39.
B32	—	solid	32	4	328	1.28	1.6	1.6	42.	6.76	10.	6.9	21.	8.3	1.6	39.
B32w	ent wa	solid	32	4	328	1.28	1.6	1.6	42.	5.44	10.	6.5	19.	9.6	2.2	30.
B32w'	ent'wa	solid	32	4	328	1.28	1.6	1.6	42.	5.44	10.	6.1	—	9.7	2.2	49.
B32c	ent co	solid	32	4	328	1.28	1.6	1.6	42.	0.05	10.	6.5	19.	9.6	2.1	29.
B32^{5}c	ent co	solid	32	5	656	1.28	1.6	1.6	42.	0.05	24.	14.	18.	4.5	1.9	30.
B64	—	solid	64	4	328	0.64	1.6	1.6	42.	6.25	10.	5.7	25.	9.2	2.4	39.
B64c	ent co	solid	64	4	328	0.64	1.6	1.6	42.	0.05	10.	5.5	25.	9.1	2.4	40.
C32c	ent co	anti	32	4	328	1.28	1.6	1.6	42.	0.05	10.	4.2	1.7	0.13	0.005	58.
C64c	ent co	anti	64	4	328	0.64	1.6	1.6	42.	0.05	10.	5.7	6.0	0.35	0.0085	69.
C128c	ent co	anti	128	4	328	0.32	1.6	1.6	42.	0.05	2.	>0.3	>1.	>0.	>0.	78.
O32	—	oppo	32	4	328	1.28	1.6	1.6	42.	0.05	10.	4.0	9.0	1.57	0.36	66.
O64	—	oppo	64	4	328	0.64	1.6	1.6	42.	0.05	10.	3.4	8.4	1.19	0.19	89.
S32	—	solid	32	4	328	1.28	1.2	1.2	42.	4.68	11.6	6.0	16.	7.9	2.4	32.
S64	—	solid	64	4	328	0.64	1.2	1.2	42.	4.71	10.	6.5	23.	7.5	2.0	35.
D32	—	solid	32	4	400	1.56	1.8	1.2	46.	7.16	10.	7.1	14.	8.8	2.7	39.
D64	—	solid	64	4	400	0.78	1.8	1.2	46.	7.19	13.	7.0	13.	9.3	3.8	35.
D64^3	3 grids	solid	64	3	400	1.56	1.8	1.2	46.	7.16	5.	>2.7	22.	>0.8	>0.4	>33.
D128^3	3 grids	solid	128	3	400	0.78	1.8	1.2	46.	7.19	2.	>0.2	>5.	>0.	>0.	>12.

try to reduce it by localizing grid cells with temperature spikes in the shocked region below a certain density and resetting the temperature there to an average value of the surrounding grid zones. The influence of this manipulation has to be tested. On the one hand we did this by computing models with increasingly better resolution (where the disturbing effects occured in a smaller volume of space), on the other hand we changed the procedure for detecting the zones with unphysical temperatures. A corresponding test model is B32w'.

4. Results

In this section the results of our new simulations will be described as far as important differences to our previously published models showed up, or interesting effects occurred in dependence of the parameters varied between the models.

4.1. Dynamical evolution and gravitational-wave emission

Figures 2–7 show the hydrodynamical results for five of the models listed in Table 1. The displayed cases include Model A64 with two equal, initially nonrotating neutron stars (Fig. 2), Model B64 with two equal, initially corotating stars (Fig. 3), Model C64 with two equal, initially counterrotating stars (Fig. 4), Model O64 with equal neutron stars with the spins pointing in opposite directions (Fig. 5), and Model D64 with neutron stars of different masses in initially locked rotation (Fig. 6). Figure 7 provides cuts perpendicular to the orbital planes for Models B64, O64, and D64, whereas the other plots display the density and temperature distributions in the orbital plane.

Compared to our previously published simulations (Ruffert et al. 1996, 1997a), Models A64, B64, and C64 were computed with a finer resolution around the grid center and simultaneously a significantly larger volume by employing nested grids. Corresponding models with 32 zones on the finest grid level have a similar resolution as the standard models in our preceding papers. In addition, Model C64 was started with a lower initial temperature and the temperature history was followed by using the entropy equation.

The displayed results reveal a significant dependence of the dynamical evolution on the neutron star masses
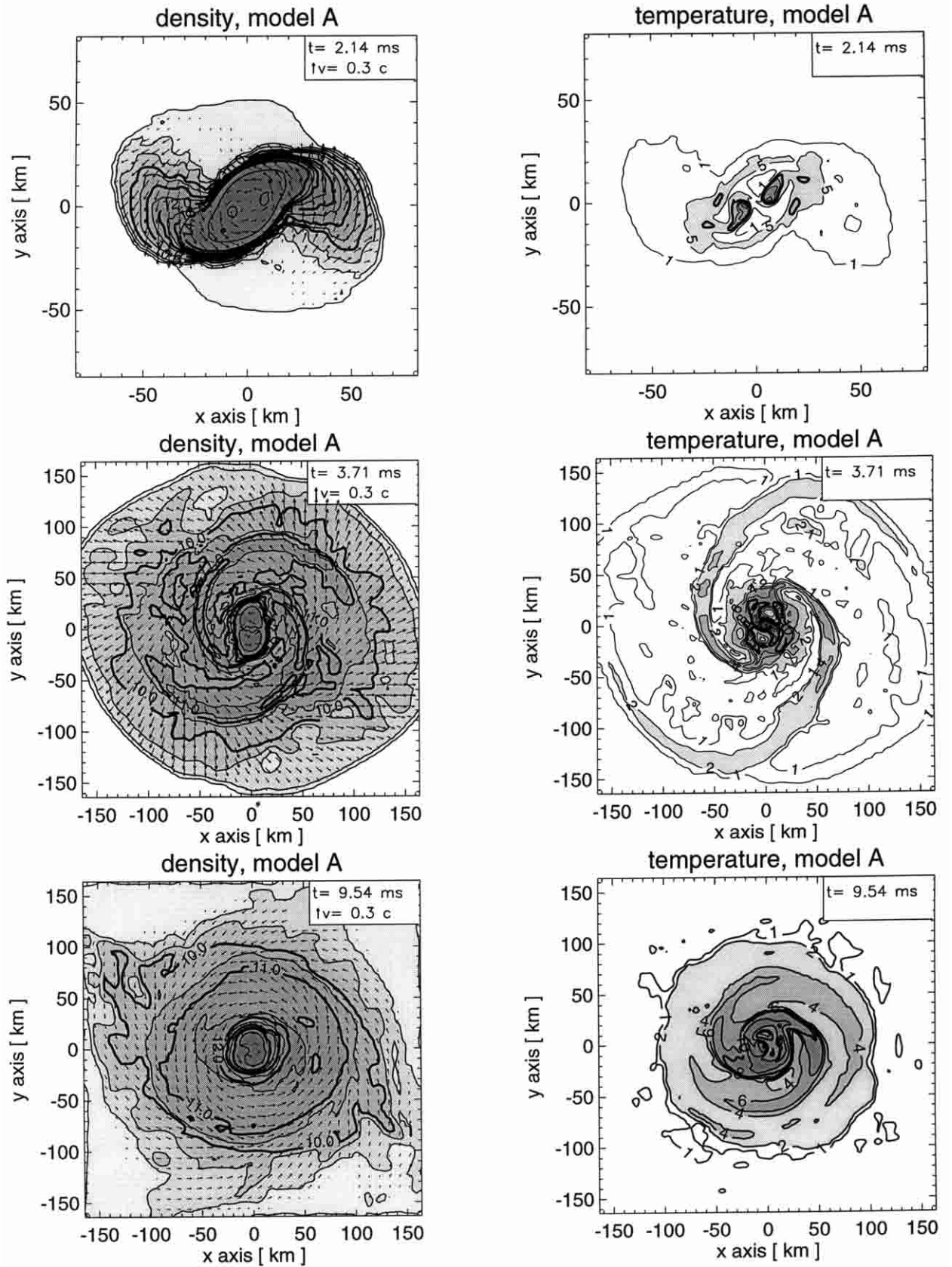
density, model A

temperature, model A

density, model A

temperature, model A

density, model A

temperature, model A

Fig. 2. Density (left) and temperature (right) distribution in the orbital plane of Model A64 for different times after the start of the simulation. The arrows in the density plots indicate the velocity field. The density is given in $\mathrm{g\,cm^{-3}}$ with contours spaced logarithmically in steps of 0.5 dex. The temperature is measured in MeV, its contours are labeled with the corresponding values, the bold contours being 10 MeV, 20 MeV, etc. Note the different scales of the axes of the plots for different times.
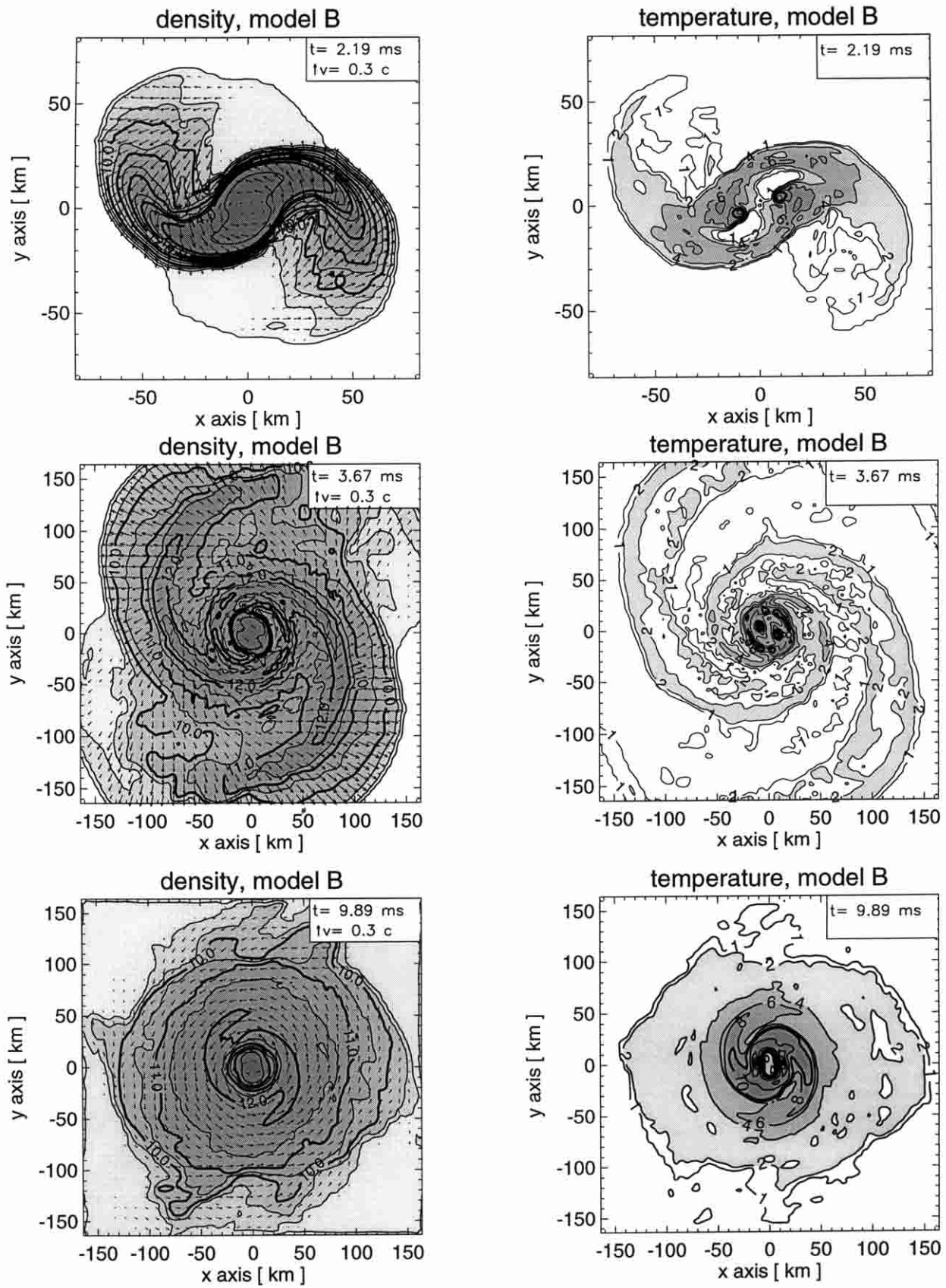
Fig. 3. Same as Fig. 2, but for Model B64.
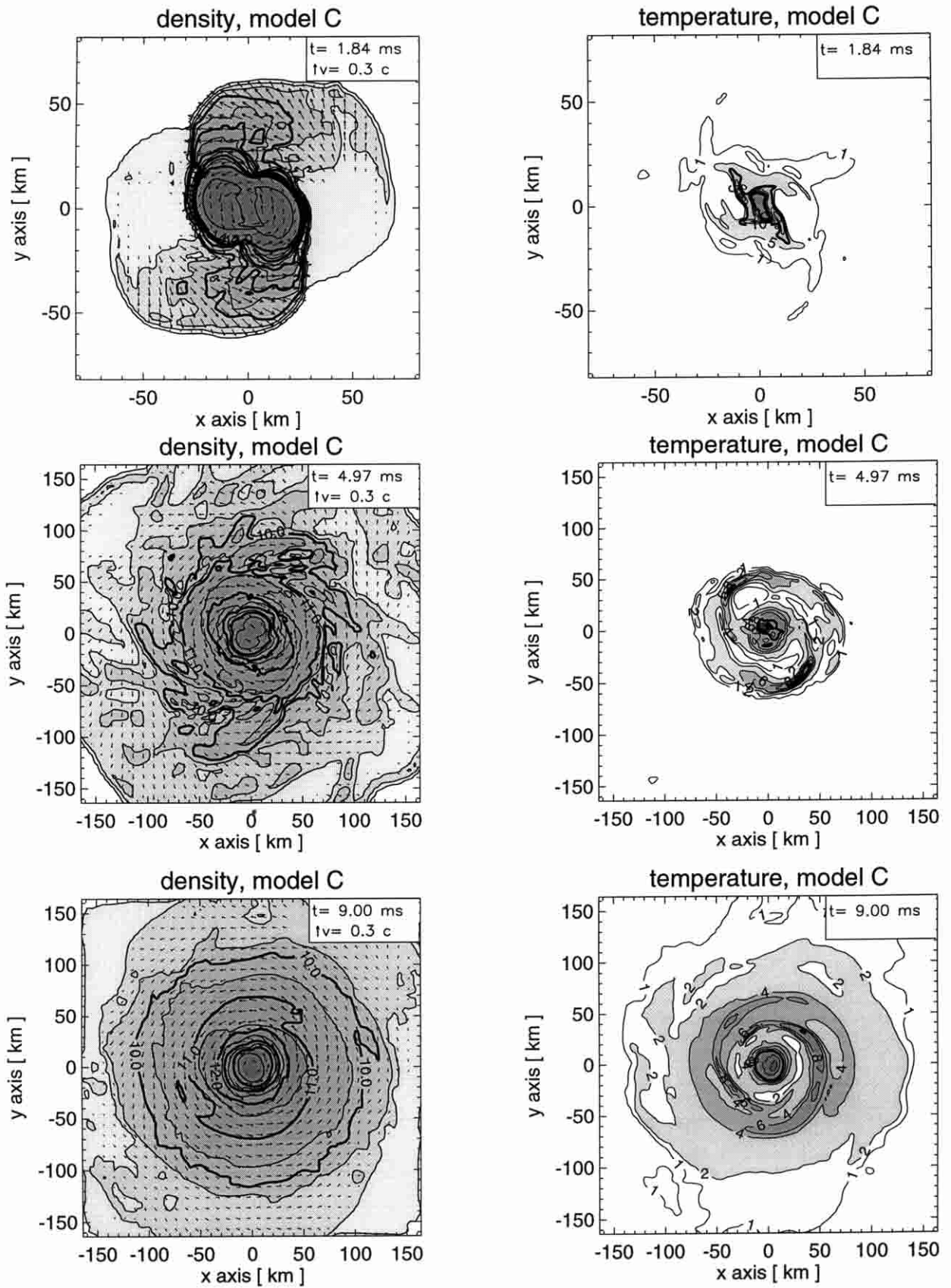
Fig. 4. Same as Fig. 2, but for Model C64c.
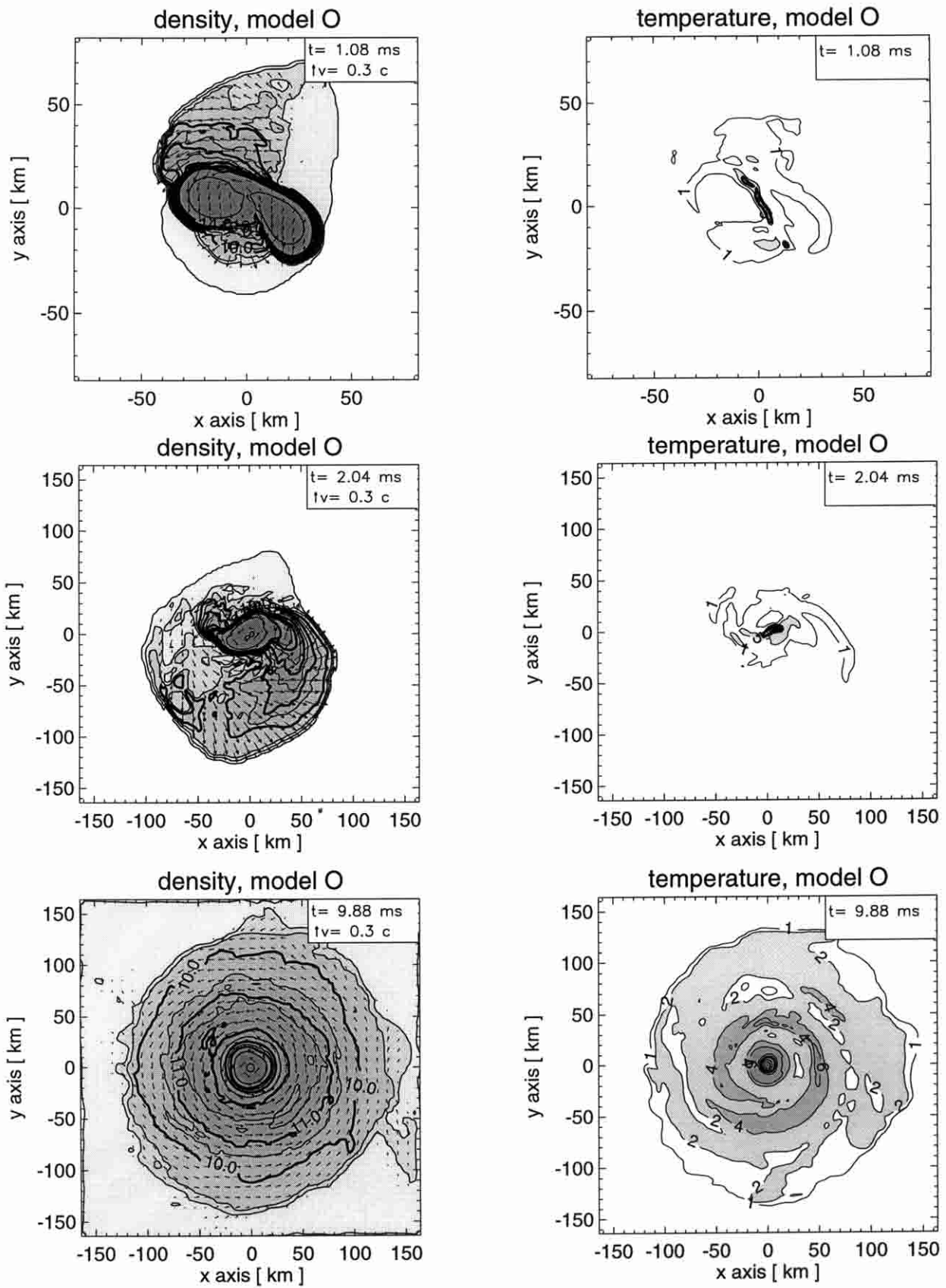
Fig. 5. Same as Fig. 2, but for Model O64.
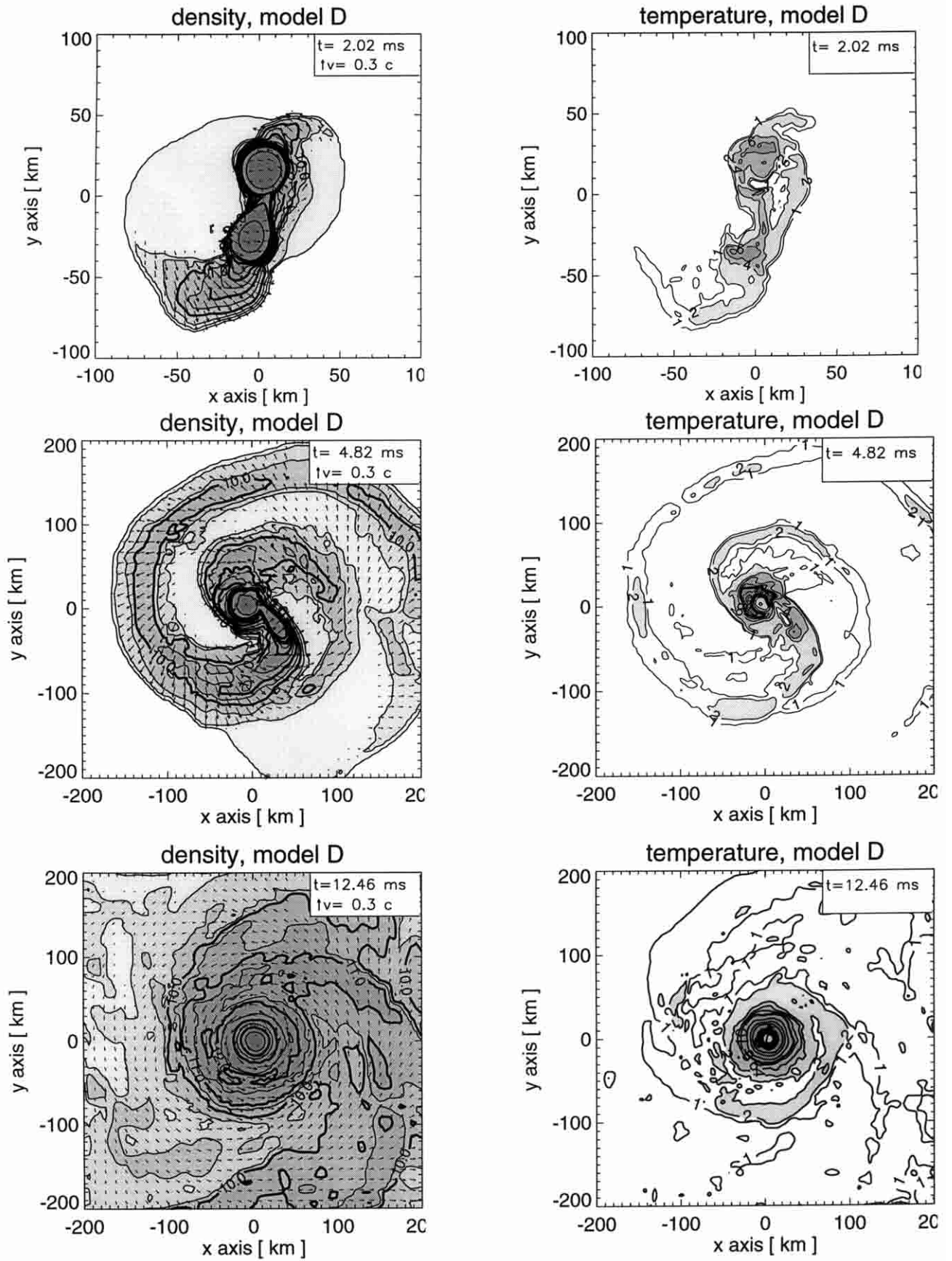
Fig. 6. Same as Fig. 2, but for Model D64.
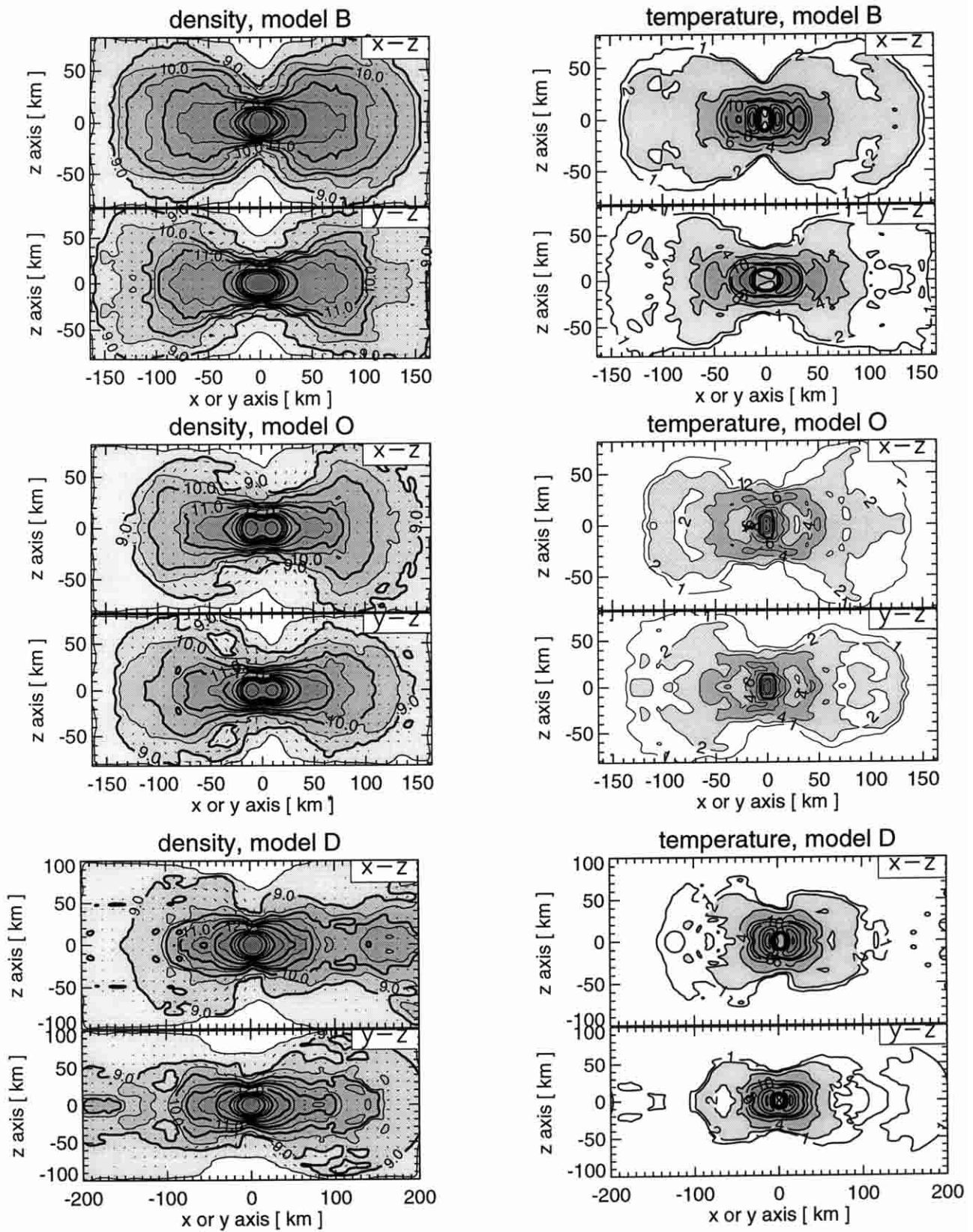
Fig. 7. Density (left) and temperature (right) in the x–z–plane and y–z–plane perpendicular to the orbital plane at the end of the computed evolution of Models B64, D64, and O64. The plots correspond to the last moments shown in Figs. 2–4, respectively.

and spins. In the corotating case (B64) pronounced spiral arms form, which are much less strongly developed in the A and C models and are present only for the corotating component in Model O64. In case of the different neutron star masses (D64) the less massive star is stretched to a long, banana shaped object before it is finally wrapped around the more massive component. Prior to this, a sizable amount of matter is flung out from the outward pointing end of the smaller star. This material forms a spiral arm which expands away from the merger site.

The initial total angular momentum of the binary systems varies with the spins of the two components. Among the models with the same masses of the two neutron stars, the total angular momentum is largest for the B cases (neutron stars corotating with the orbit), smaller for the A (no neutron star spins) and O models (spins in opposite directions), and smallest for the C models (both neutron stars in counterrotation with the orbital motion) (Fig. 8). During the computed evolution, about 10% of the angular momentum are removed by the emission of gravitational waves (Fig. 8). This leads to correlations between maxima of the gravitational-wave luminosity and periods of a decrease of the angular momentum on the grid (compare Figs. 8 and 11). More angular momentum is carried away by the matter that leaves the boundaries of the computational grid. While the gravitational-wave emission peaks within the first 2 milliseconds, the effect due to the mass loss becomes important only later than 4–6 ms after the start of the simulations. In addition, the code does not conserve the angular momentum exactly. The violation depends mainly on the resolution of the finest grid level, where the bulk of the matter is located. For the models with a cell size of 0.64 km on the central grid, less than 10% of the initial angular momentum were destroyed within about 10 ms of evolution. This, unfortunately, does not reach the excellent quality of the conservation of energy by our code (Fig. 9).

The total angular momentum of the coalescing binary system determines the structure and the dynamical state of the very compact central body of the merger remnant, which contains the bulk ($\gtrsim 90\%$) of the system mass. The wobbling and ringing of this body after the merging is sensitive to the fluid motions and thus to the value and distribution of angular momentum in its interior. The plots in Fig. 10 show that the two stars in Model B64 fuse smoothly and form a centrally condensed body immediately after the plunge, whereas in Model A64, and even stronger in Model C64, two density maxima can still be distinguished later. In particular in the counterrotating Model C64 the distance of these density maxima varies with time, indicating that the remnant remains in a perturbed internal state. Correspondingly, the gravitational waveform of Model C64 (Fig. 12) reveals a low-freqency modulation on top of the high-frequency structure which is caused by the oscillation period of the compact remnant. This feature is essentially absent in Model B64.

Before the final plunge, which is marked by the maxima of the gravitational waveforms, the gravitational wave
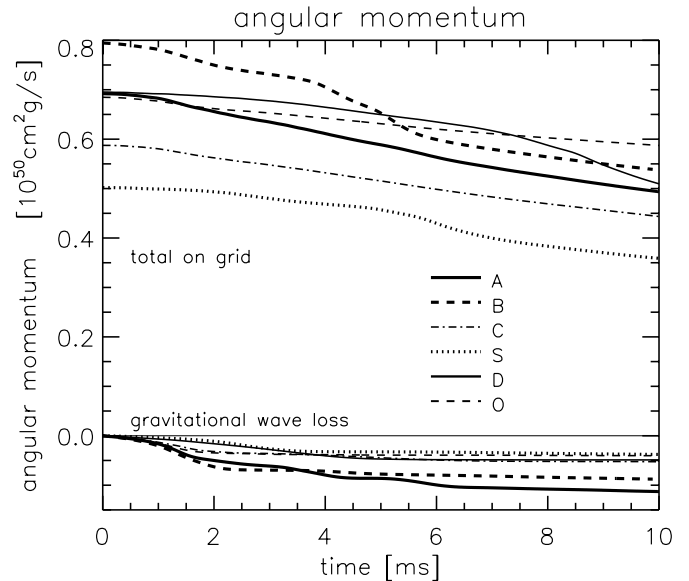

Fig. 8. Total angular momentum (component perpendicular to the orbital plane) of the matter on the grid (upper curves) and cumulative angular momentum loss by gravitational wave emission (lower curves) as functions of time for different models.

emission follows the chirp signal of two point masses rather accurately. We have not started our simulations with a configuration in rotational equilibrium and correspondingly deformed neutron stars. Therefore the neutron stars oscillate around their new quasi-equilibrium state before the merging, and the density maximum on the grid shows periodic modulations. Although these internal pulsations of the two stars are not damped by numerical viscosity (which expresses the non-dissipative quality of the code; Fig. 10), they do not have any visible consequences for the gravitational waveforms.

The deviation from the chirp signal becomes large when the orbital instability sets in and the neutron stars get strongly deformed and finally begin to touch each other. This moment contains very important information about the properties of the neutron stars, in particular about their mass-radius relation, which depends on the stiffness of the nuclear EoS. Similarly important and characteristic information about the binary system is carried by the post-merging signal, which is emitted if the massive and compact merger remnant is stabilized by pressure or centrifugal forces and does not collapse to a black hole on a dynamical timescale. The collection of gravitational-wave amplitudes displayed in Fig. 12 supports this argument. The waveforms for the binary systems vary strongly with the spins of the neutron stars (compare Model O with Models A, B, and C) and with the mass ratio of the two stars (Model D). Of course, following the post-merging evolution definitely requires a general relativistic description of the problem, and quantitatively meaningful predictions of the gravitational-wave emission cannot be made on grounds of our basically Newtonian simulations. Relative differences between the models in dependence of
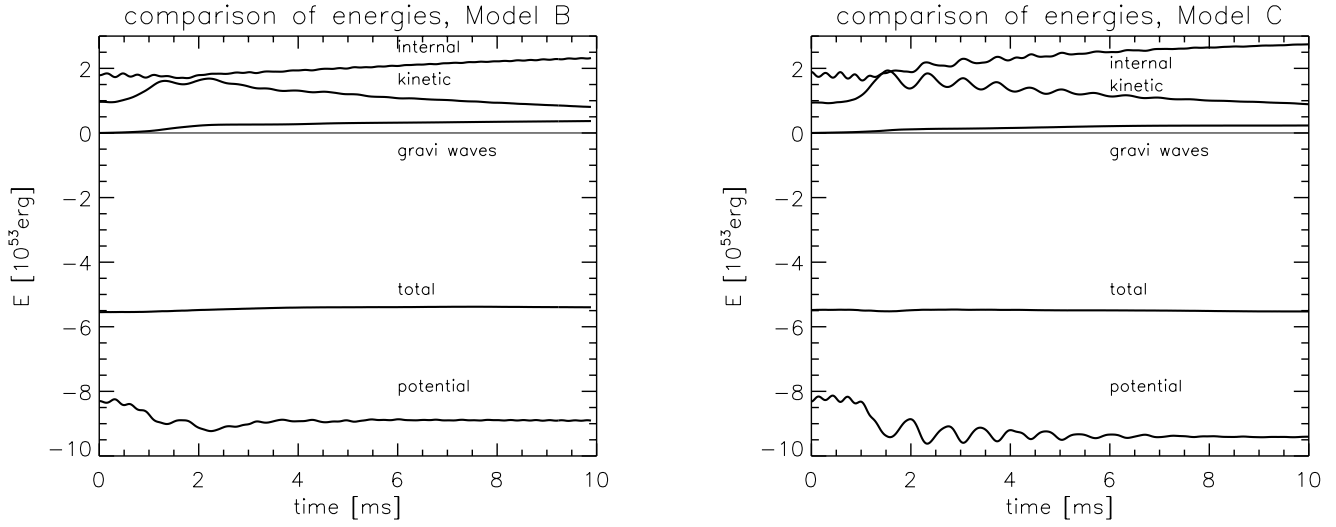
Fig. 9. Total internal, kinetic, and gravitational potential energies of the matter on the grid as functions of time for Models B64 and C64c. The total energy is calculated by adding up these energies plus the energy that was emitted in gravitational waves. It should be conserved, because the gas that leaves the grid, has a total energy very close to zero.
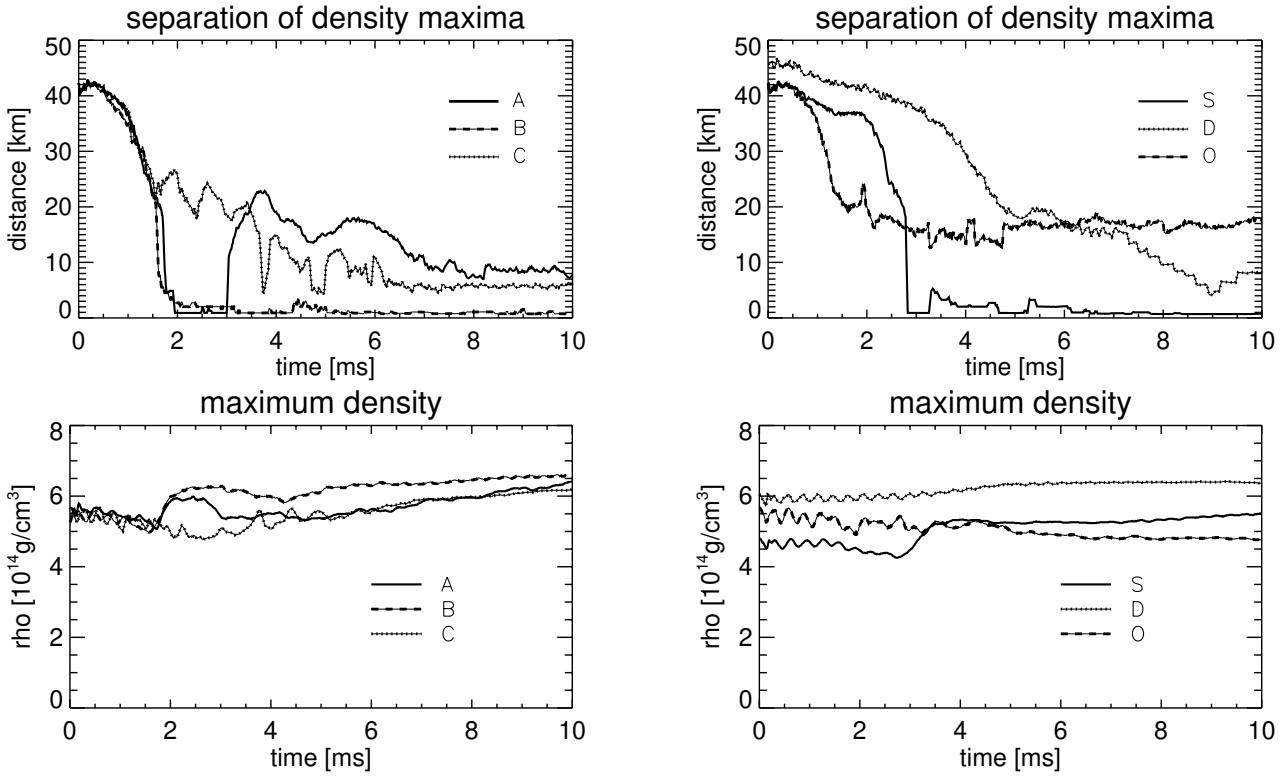

Fig. 10. The separation of the density maxima and the values of the maximum density on the grid as functions of time for different models.

the binary parameters should, however, also survive in a relativistic treatment.

Comparison of the gravitational-wave amplitudes of Models A64, B64, and C64 with results displayed in Fig. 25 of Ruffert et al. (1996) reveals discrepancies for the post-merging signals. Because of the better numerical resolution of our present simulations (the cell size on the finest grid is 0.64 km instead of 1.28 km for the old models), the numerical loss of angular momentum is

significantly lower now. The influence of the resolution can be directly tested by Models A32, B32, and C32, which have a factor of two larger cells on the innermost grid and thus have the same resolution as the old calculations. The structure of the wave amplitude for Models A32, B32, and C32 is therefore much more similar to our previously published results.

The gravitational-wave luminosity (Fig. 11) peaks when the two neutron stars plunge into each other and the
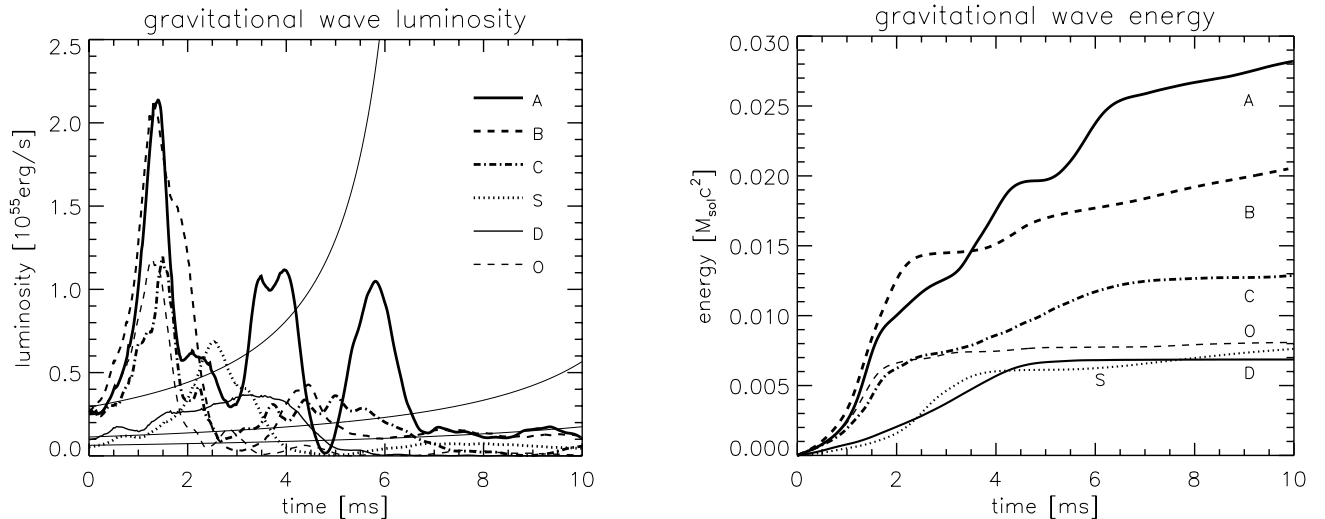
Fig. 11. Gravitational-wave luminosity and cumulative energy emitted in gravitational waves as functions of time for different models. The thin solid curves represent the emission of binary systems with two point masses instead of the neutron stars.

quadrupole moment of the binary changes most rapidly. For Models A, B, C, O this happens at roughly the same time, but the maximum luminosity of Models A and B is about twice as large as the one of the counterrotating Model C and of Model O where the neutron star spins are in opposite directions. Model S with smaller neutron stars and Model D with different neutron stars show significantly lower peak luminosities. For a short time, the luminosity rises above the value of two orbiting point masses at the same distance. Because of the finite size of the neutron stars and the rapid development of a nearly spherical merger remnant, however, the luminosity decreases quickly after the maximum and never diverges as in case of the arbitrarily close approach of point masses. In the cases with strong, coherent fluid motion within the remnant, secondary and even tertiary maxima can occur. Such effects are absent in Model D and very weak in Model O.

Our models are basically Newtonian, therefore the calculated gravitational waveforms are of limited usefulness as templates for measurements. Nevertheless, the simulations can serve for comparison with future, fully general relativistic models and will help one understanding the properties of their gravitational-wave signals.

4.2. Dynamical mass loss

Immediately after the merging of the neutron stars, tidal arms begin to reach out through the outer Lagrange points of the binary system. A little later, between 3 and 6 milliseconds after the start of the simulations, these spiral arms become inflated, because the matter expands with radial velocities up to one third of the speed of light. At that time the spiral arms reach the boundaries of the computational volume and mass flows off the grid in our simulations. This phase coincides roughly with the moments shown in the middle panels of Figs. 2–6 and can be recognized in Fig. 13 from the steep increase of the plotted

curves. We monitor the fraction of the matter which fulfills the condition that its total specific energy as the sum of gravitational, kinetic and internal energies is positive. This matter is considered to potentially become unbound.

The amount of matter which is stripped off the tips of the spiral arms depends on the total angular momentum of the coalescing binary system. For solid-body type initial rotation we find the largest values: roughly a tenth of a solar mass leaves the grid, and about 20–30% of this matter might escape the system. The mass ejection is roughly a factor of ten smaller for the cases of irrotational neutron stars and neutron star spins in opposite directions, and another factor of ten smaller for the configuration with initially counterrotating stars (Table 1 and Fig. 13).

The gas mass M_g that is swept off the grid and the mass M_u that may get unbound exhibit only a rather weak dependence on the grid resolution, which can be seen by comparing models with different choices of grids in Table 1. Of course, the size of the largest grid has a significant influence on M_g, but again does not affect M_u very much (Model B32^{5}c).

Although the correlation of mass ejection with the angular momentum of the binary system appears plausible, and basically is consistent with the results of Rosswog et al. (2000), we cannot claim to have determined final values for the dynamical mass loss. There are several factors of uncertainty which affect our numbers. The finite environmental gas density, which we have to assume around the neutron stars for numerical reasons, has probably negligible dynamical influence. More problematic is the decreasing resolution of the nested grids towards the boundaries of our computational volume. The largest uncertainty, however, is connected with the fact that we cannot follow the expanding matter until it moves ballistically. Therefore it is unclear how efficiently internal energy is finally converted into bulk kinetic energy by hydrodynamical effects (i.e., PdV-work). Our results for the
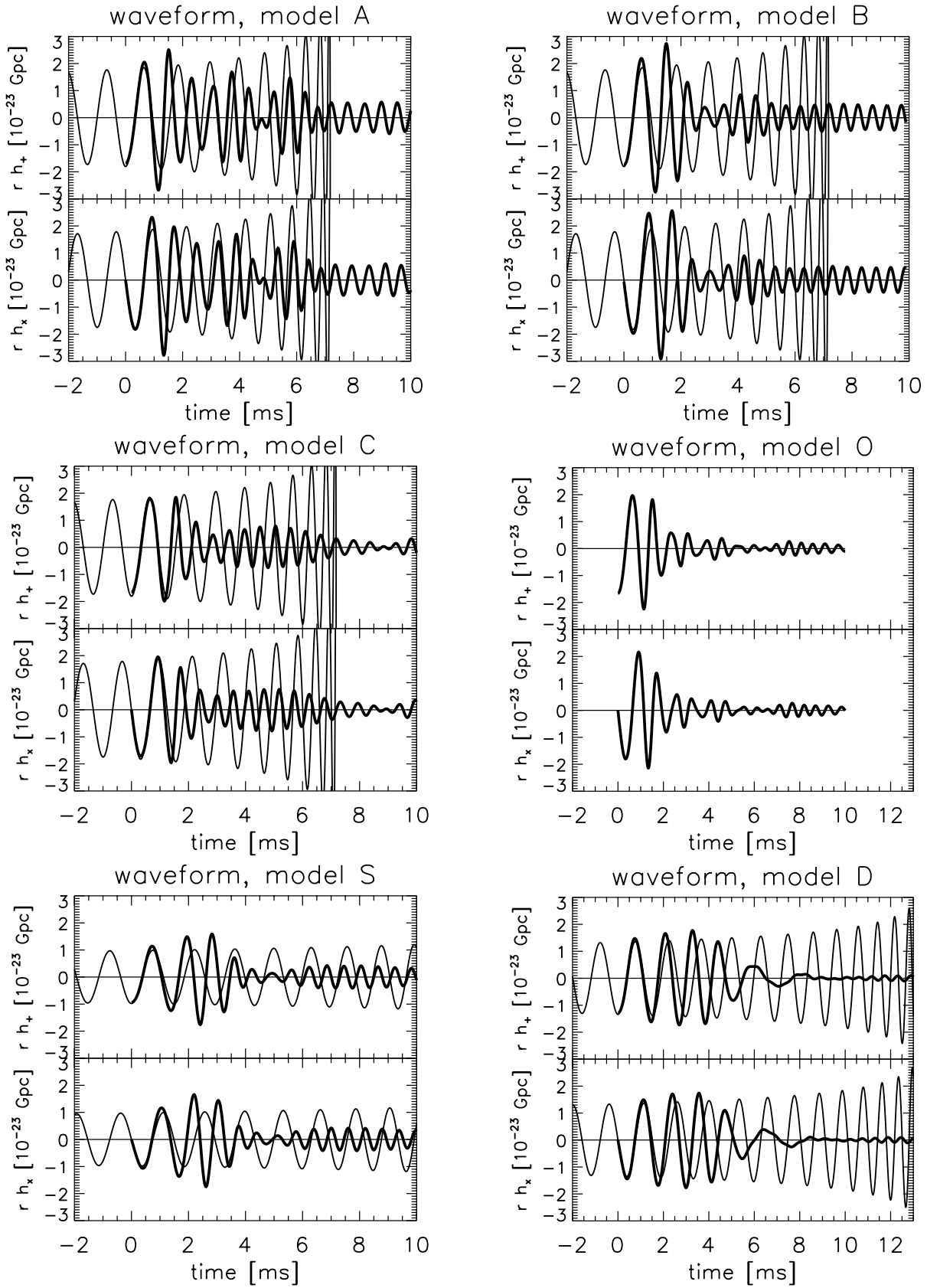
Fig. 12. Gravitational waveforms of Models A64, B64, C64, O64, S64, and D64. Time is measured in milliseconds from the start of the simulations, the observer is located perpendicular to the orbital plane. The thin solid lines correspond to the chirp signal of two point masses.
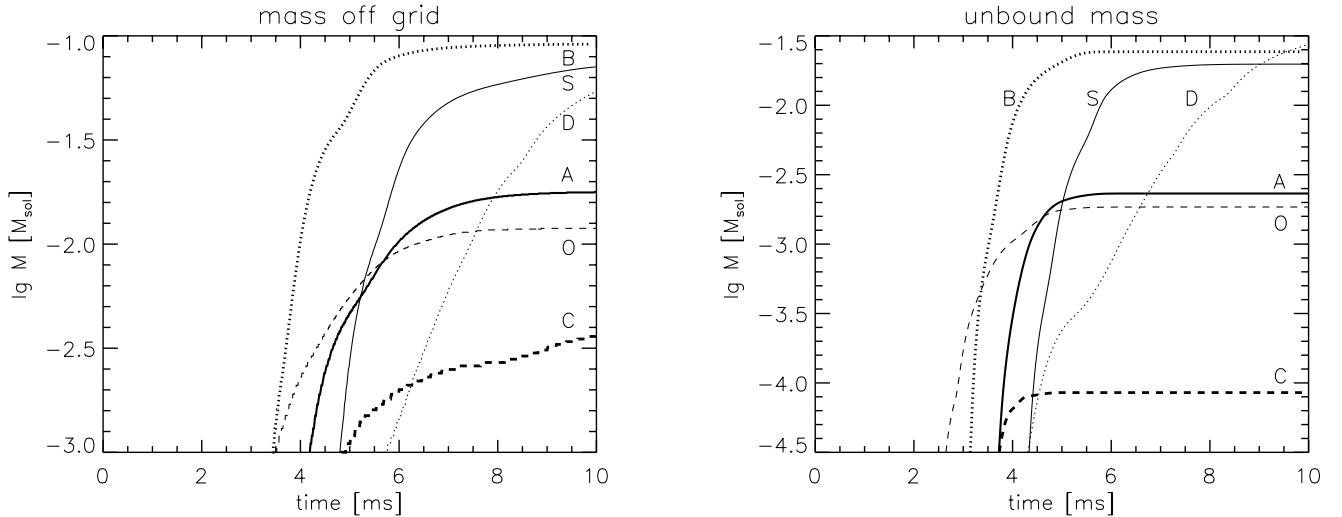
Fig. 13. The cumulative amount of gas that flows off the grid as function of time for different models (left) and the amount of matter that is estimated to become unbound, because its total energy (as the sum of gravitational, kinetic, and internal energies) is positive.

Table 2. Gravitational-wave and neutrino emission properties for all models. $\widehat{\mathcal{L}}$ is the maximum gravitational-wave luminosity, $\mathcal{E}$ is the total energy emitted in gravitational waves, $\widehat{rh}$ is the maximum amplitude of the gravitational waves scaled with the distance to the observer, r, L_{ν_e} is the electron neutrino luminosity after approaching a saturation level at about 8 ms, $L_{\bar{\nu}_e}$ is the corresponding electron antineutrino luminosity, and L_{ν_x} the luminosity of each individual species of heavy-lepton neutrinos, $\langle \epsilon_{\nu_e} \rangle$, $\langle \epsilon_{\bar{\nu}_e} \rangle$ and $\langle \epsilon_{\nu_x} \rangle$ are the mean energies of the emitted ν_e, $\bar{\nu}_e$, and ν_x, respectively. L_ν gives the total neutrino luminosity at the end of the simulation and $\dot{E}_{\nu\bar{\nu}}$ denotes the integral rate of energy deposition by neutrino-antineutrino annihilation.

model	$\widehat{\mathcal{L}}$ $10^{55} \frac{\text{erg}}{\text{s}}$	$\mathcal{E}$ 10^{52} erg	$\widehat{rh}$ 10^4cm	L_{ν_e} $10^{53} \frac{\text{erg}}{\text{s}}$	$L_{\bar{\nu}_e}$ $10^{53} \frac{\text{erg}}{\text{s}}$	L_{ν_x} $10^{53} \frac{\text{erg}}{\text{s}}$	L_ν $10^{53} \frac{\text{erg}}{\text{s}}$	$\langle \epsilon_{\nu_e} \rangle$ MeV	$\langle \epsilon_{\bar{\nu}_e} \rangle$ MeV	$\langle \epsilon_{\nu_x} \rangle$ MeV	$\dot{E}_{\nu\bar{\nu}}$ $10^{50} \frac{\text{erg}}{\text{s}}$
A32	2.3	4.9	8.6	0.8	2.0	0.43	4.5	12.	18.	27.	—
A64	2.1	5.2	8.6	0.9	2.6	0.37	5.0	11.	17.	27.	90.5
B32	2.2	3.8	9.2	0.6	2.3	0.45	4.7	12.	17.	25.	—
B32w	2.2	3.5	8.4	0.65	1.9	0.23	3.5	13.	15.	25.	—
B32w'	2.2	3.5	8.4	0.39	1.3	>0.08	2.0	11.	15.	22.	—
B32c	2.1	3.5	8.4	>0.45	1.5	>0.09	>2.3	11.	15.	22.	—
B32^{5}c	2.1	3.7	8.3	0.65	1.0	0.08	1.9	12.	16.	23.	—
B64	2.1	3.7	8.9	0.6	1.8	0.22	3.3	12.	17.	25.	70.0
B64c	2.1	3.6	8.5	>0.62	>1.6	>0.07	>2.5	13.	16.	24.	—
C32c	0.85	3.4	6.0	>1.0	>2.2	>0.2	>4.0	11.	16.	27.	—
C64c	1.2	2.3	6.0	>1.1	2.3	0.13	>4.0	11.	16.	26.	—
O32	1.3	1.5	6.9	0.4	0.9	0.02	1.4	12.	19.	23.	—
O64	1.2	1.5	6.9	0.4	1.1	0.02	1.6	14.	17.	24.	—
S32	0.65	1.4	5.2	0.4	1.2	0.18	2.3	11.	16.	25.	—
S64	0.70	1.4	5.5	0.3	0.9	0.07	1.5	11.	16.	25.	—
D32	0.46	0.96	5.8	0.4	1.4	0.19	2.6	12.	17.	24.	—
D64	0.37	1.25	5.5	0.4	1.0	0.16	2.0	12.	19.	26.	—

ejected mass can only be considered as best estimates, supported by the fact that the expansion of the tidal tails is mainly a kinematic effect and only to a minor degree driven by pressure forces.

Matter which is ejected during the merging of binary neutron stars may have important implications for the production of heavy elements in our Galaxy. Dynamical events involving neutron stars (mergers, explosions) have been speculated to be possible sources of *r*-process

nuclei, both because of the high neutron densities present in the interior of neutron stars and because of the neutron-rich nuclei which exist in the crust below the surface of the cold neutron star (e.g., Hilf et al. 1974; Lattimer & Schramm 1974, 1976; Lattimer et al. 1977; Symbalisty & Schramm 1982; Eichler et al. 1989; Meyer 1989; Freiburghaus et al. 1999). The crust below a density of about 2×10^{14} g cm^{-3} (see, e.g., Weber 1999) can contain up to several hundredths of a solar mass for a neutron
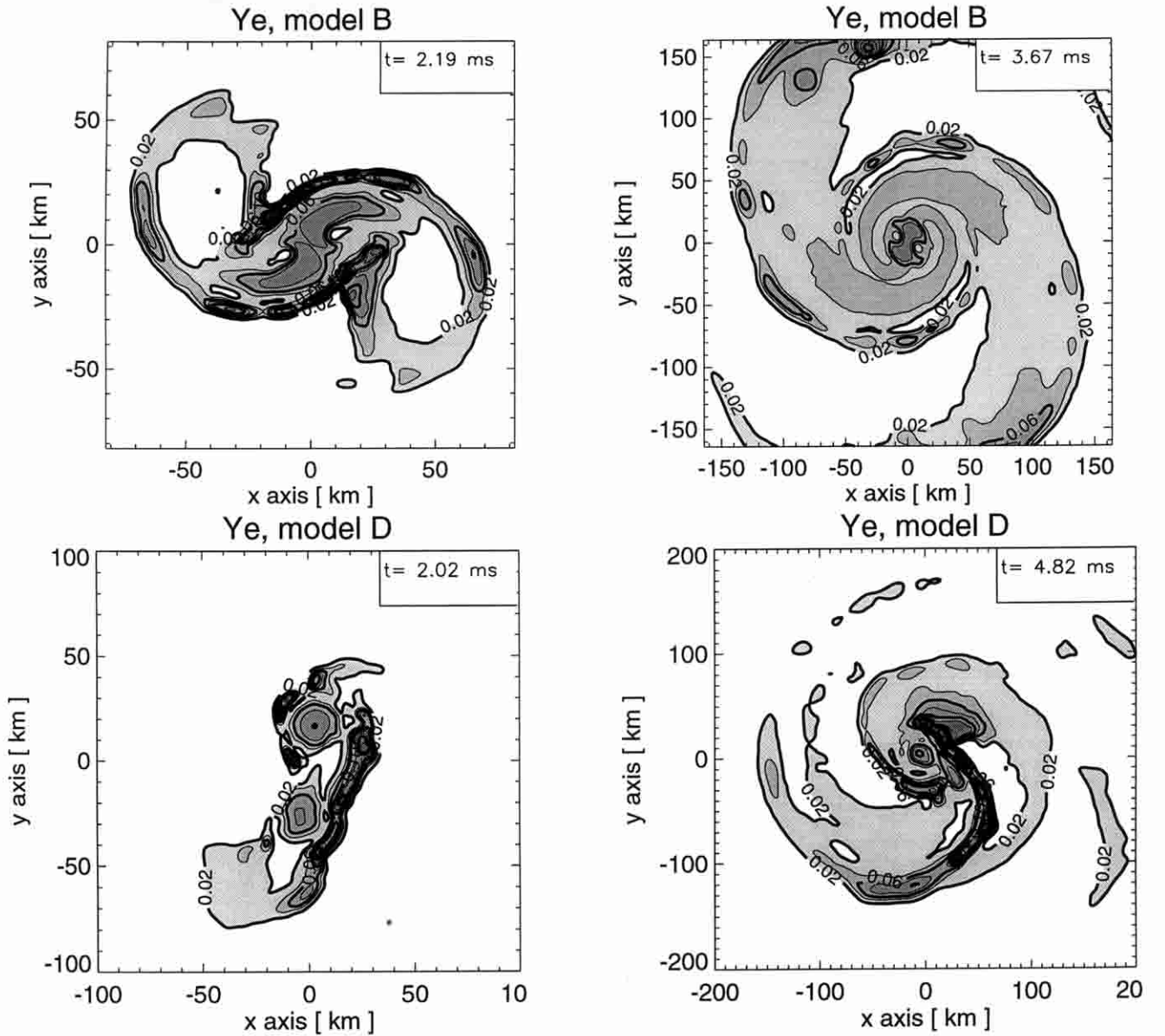
Fig. 14. Electron fraction Y_e in the orbital plane at two different times for Model B64 (upper row) and Model D64. The contours are spaced linearly in steps of 0.02, beginning with a minimum value of 0.02, which is also adopted for the very dilute environmental medium. The bold lines correspond to values of 0.02, 0.06, 0.1, 0.16, 0.2, and 0.3. The maximum values are 0.28 in the upper left plot, 0.18 in the upper right one, 0.35 in the lower left one, and 0.33 in the lower right one.

star with a gravitational mass around $1.4 \, M_\odot$ (e.g., Akmal et al. 1998), although the exact value is somewhat EoS dependent. With an estimated merger rate of one per $10^{5\pm1}$ years and a mean mass loss per event of $\sim 10^{-3}$ solar masses, about 10–1000 solar masses of r-process material might have been produced by 10^4 to 10^6 such events over the history of our Galaxy.

Quantitative predictions of the abundance yields are not easy to obtain. Ideally, the nuclear reactions and beta decays of neutron-rich isotopes should be followed along with the hydrodynamic flow of the expanding ejecta, because heating by beta decays and neutrino losses can influence their thermal and chemical evolution. Moreover, it is essential to start the nucleosynthesis calculations with

appropriate initial conditions. This concerns the initial temperature, initial electron fraction $Y_e = n_e/n_b$, and the initial nuclear composition of the surface material of cold neutron stars.

A first attempt for a nucleosynthetic evaluation of the merger ejecta was performed as a post-processing step of hydrodynamical data (Freiburghaus et al. 1999). Instead of being self-consistently determined as the consequence of neutrino reactions, the electron fraction was set to a chosen value. In addition, the initial temperature of the ejected neutron star matter was considered to be high enough ($T \gtrsim 5 \times 10^9$ K) for the composition to be determined by nuclear statistical equilibrium (NSE). This is not necessarily a correct assumption, because the matter that

is flung out in the tidal arms is not subject to any heating processes which could significantly increase the surface temperature of the originally cold neutron stars. In three-dimensional hydrodynamical simulations of neutron star mergers, however, the limited numerical resolution does not allow one to accurately trace the thermal history of such cold matter, but numerical viscosity und numerical noise lead to artificial heating (for our code, such problems are discussed in Sects. 2 and 3). If the temperature stays low, which is most likely the case in the ejected and decompressed matter, the initial nuclear composition of the neutron star crust is not erased by the onset of NSE. Instead, the neutron-rich nuclei start to undergo beta decays and the final distribution of stable or long-living nuclei is sensitive to the initial composition (e.g., Hilf et al. 1974; Lattimer et al. 1977; Meyer 1989; Sumiyoshi et al. 1998).

In our simulations the electron fraction evolves as a result of the emission of electron neutrinos ν_e and antineutrinos $\bar{\nu}_e$. Near the tips of the tidal tails, however, the neutrino producing reactions are not fast enough to cause a sizable change of the initial value of Y_e on the short timescales of the dynamic expansion. This is so because the temperature near the neutron star surface was chosen to be "only" around 1–2 MeV in the beginning (see Fig. 2 in Ruffert et al. 1996; such values of the temperature are certainly unphysically high for cold initial stars, but they can be considered as low for the present discussion) and the temperature does not increase in the spiral arms during the subsequent evolution (Figs. 2–6). As a consequence, Y_e can serve as a tracer quantity, and our results indicate that only matter that was initially located close to the surfaces of the original stars is ejected during coalescence. This matter essentially retains its initial, very neutron-rich state with Y_e significantly less than 0.1 (which corresponds to the neutrinoless beta-equilibrium (or beta-stable) state of cold matter in the crust below the very thin envelope of a neutron star). The typical electron fraction of the ejecta is found to be around 0.02–0.04 (Fig. 14), much lower than determined by Freiburghaus et al. (1999) as favorable for an r-processing that leads to a solar-like abundance distribution. We remind the reader here, however, that the original EoS by Lattimer & Swesty (1991) does not provide values below $Y_e = 0.03$, and we use a simple extrapolation of the EoS in this regime. In fact, the exact value of Y_e in the neutron star crust is not well known because of uncertainties in the physics, for example associated with the nucleon symmetry energy or with phase transitions due to isospin states in case of very low Y_e. In addition, the current grid zoning of our three-dimensional models does not allow us to resolve the thin crust and envelope of the cold initial neutron stars, where the state of neutrinoless beta-equilibrium corresponds to a positive gradient of Y_e and thus higher values of Y_e towards the surface.

The question of dynamical mass loss is not unequivocally answered on grounds of our simulations or those of Rosswog et al. (1999, 2000). A source of uncertainty
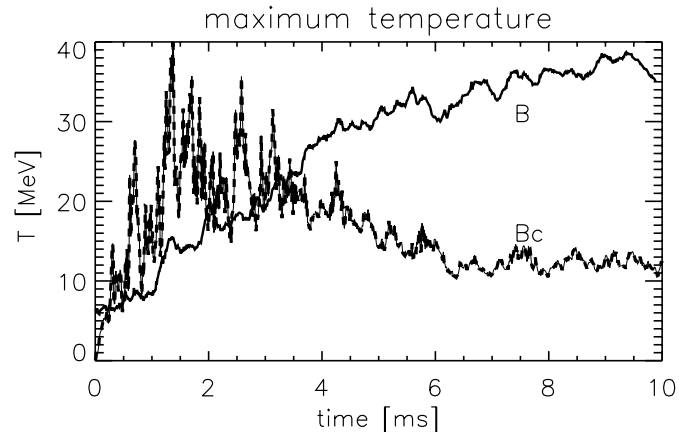

Fig. 15. Maximum temperature on the grid as a function of time for Models B64 and B64c.

is the nuclear EoS which determines the structure and properties of the merging neutron stars and the dynamics of the merging process. Rosswog et al. (2000) found that the mass loss is sensitive to the stiffness of the EoS. In particular the conditions in the supranuclear regime are highly uncertain. EoSs which have been developed for supernova simulations and are particularly suitable for hydrodynamic modeling as described here (because they provide all the required information in essentially all interesting regions of the parameter space), in particular the EoS of Lattimer & Swesty (1991) and Shen et al. (1998), do actually not include a detailed microphysical description of the regime beyond about twice the density of the nuclear phase transition. New hadronic degrees of freedom (e.g., a phase with pions, kaons or hyperons) or quark matter could be present there and would soften the EoS. While probably not crucial for stellar core-collapse and supernova simulations, this density regime determines the cooling evolution of new-born neutron stars and should also affect the merging of neutron stars. For example, if the supranuclear EoS is sufficiently soft, the maximum mass of stable (nonrotating) neutron stars can be as low as 1.5–1.6 $M_\odot$. This possibility cannot be excluded, neither on grounds of theoretical calculations of the state of matter at supranuclear densities (e.g., Weber 1999; Heiselberg & Pandharipande 2000), nor on grounds of observed neutron star masses. Although rapid and differential rotation can have a significant stabilizing influence (Baumgarte et al. 2000), such a soft EoS would probably not allow the merger remnant to escape the collapse to a black hole on a dynamical timescale (Shibata & Uryū 2001). Therefore the question will have to be investigated in more detail by future general relativistic simulations, whether in this case mass ejection, which occurs with some time delay after the final plunge, can still take place.

4.3. Thermal evolution and neutrino emission

Computing the temperature evolution is crucial for calculating the neutrino emission of the merging neutron stars.

Unfortunately, there are a number of numerical problems which affect the accuracy of the temperature determination. For our code and simulations, these problems have already been addressed in Sects. 2 and 3.

When doing simulations with a finite difference scheme, the need to assume a medium with a finite density on the computational grid constitutes a problem. In a non-rotating frame of reference (or a frame of reference which does not move with the same angular velocity as the stars), the neutron stars move through this dilute medium with a high relative velocity. This leads to shock heating at the forward surfaces of the neutron stars. We reset the temperature to lower values after each time step for densities below a certain threshold value so that only dilute material is affected by this procedure. We also detect artificially heated, isolated grid zones and reduce the local temperature by averaging over neighbouring, well behaved zones. Since only relatively few cells with a rather low density are involved, this procedure does not introduce a noticable violation of the conservation of the total energy during the simulations (Fig. 9). Moreover, the affected volume and mass decrease when the resolution is improved.

Another, more severe problem is connected with the fact that cool neutron star matter is very degenerate, i.e., the thermal energy contributes only a minor fraction to the internal energy. Since our hydrodynamics code computes the specific internal energy, from which the temperature is determined, as the difference between internal plus kinetic energy of the fluid and its kinetic energy, any small error introduced there leads to sizable perturbations in the temperature. The thus calculated temperature cannot be very accurate. For this reason, we decided to repeat some of our simulations by using an additional entropy equation, which allows us to follow the thermal history without the described sources of noise (see Sect. 2 for more details). Note that the entropy equation serves only for computing the temperature, but does not replace the energy equation as one of the conservation laws which are solved for describing the hydrodynamical flow. The neutrino source terms in the latter equation, however, are computed with the temperatures as obtained from the entropy equation.

Models B32 and B32w in Tables 1 and 2 are two cases which were computed with the same grid resolution, but in the second model the additional entropy equation was used. Both simulations were started with nearly the same temperatures in the neutron stars. The additional Model B32c represents a case where the initial central temperature was chosen to be as low as 0.05 MeV instead of 6.76 MeV in Model B32 or 5.44 MeV in Model B32w. The values for the different entries in the tables show that the dynamic quantities and the gravitational-wave emission are nearly the same. The quantity that is most sensitive to the different treatments is the mass $M_{\rm u}$ which can become unbound from the system. Despite of the different thermal evolutions, even the overall properties of the neutrino emission at the end of the computations are rather similar.

For discussing more details, let us now consider two better resolved calculations, Models B64 and B64c. These two exemplary models differ by the use of the entropy equation in combination with a low initial central temperature in Model B64c, namely 0.05 MeV instead of 6.25 MeV in the neutron stars of Model B64 (Table 1). The lower initial temperature is more realistic than our usually "warm" initial conditions, because viscous heating prior to the merging is unlikely to achieve temperatures in excess of 10^9 K (Bildsten & Cutler 1992; Kochanek 1992; Lai 1994). Starting with a cold initial state requires the use of the entropy equation (see above).

Figure 15 shows the maximum temperatures on the grid as functions of time for Models B64 and B64c. Indeed, the maximum temperatures evolve significantly differently. This is confirmed by the upper panels of Fig. 16, which show the temperature in the equatorial plane of Model B64c for two times, which can directly be compared with snapshots given for Model B64 in Fig. 3. Note that in Model B64 the maximum temperature during the early phase is limited by the spike-correction procedure, whereas such a temperature reduction is not applied to the "entropy-temperature" in Model B64c.

The different temperatures in both simulations affect the neutrino source terms for lepton number and energy, which are very sensitive to the gas temperature (see the Appendices in Ruffert et al. 1996). Since the neutrino source terms enter the hydrodynamics equations and the continuity equation for the electron lepton number, they could in principle have consequences for the dynamical evolution of the models. In reality, however, the neutrino emission is irrelevant for the dynamics, because the associated energy is too small on the short timescale of the calculation.

Although Model B64c has higher peak temperatures during the early phase of the evolution, the average temperatures are considerably lower than in Model B64 (Figs. 3 and 16). These lower temperatures reduce the (anyway small) changes of the lepton number due to the neutrino emission in the expanding tidal tails. The panels in the second row of Fig. 16 confirm that the lepton number remains essentially unchanged from its value of about 0.02 near the surfaces of the original neutron stars (compare also with Fig. 14).

The temperature distributions in the orbital plane of Models B64 and B64c at the end of the simulations (see Figs. 3 and 16) reveal that only moderate differences occur in the cloud of low-density material ($\rho \lesssim 10^{12}$–10^{13} g cm^{-3} at $r \gtrsim 50$ km) which surrounds the much denser and very compact core of the merger remnant. Shock heating has increased the temperatures in this cloud to values between 1 MeV and 5–6 MeV in both models. Much more pronounced differences between the models can be found in the interior of the compact core, where Model B64 is significantly hotter ($T > 10$–15 MeV), mainly due to the dissipation of kinetic energy by numerical viscosity. The corresponding heating depends on the shear motions, which are particularly strong during the phase when the neutron
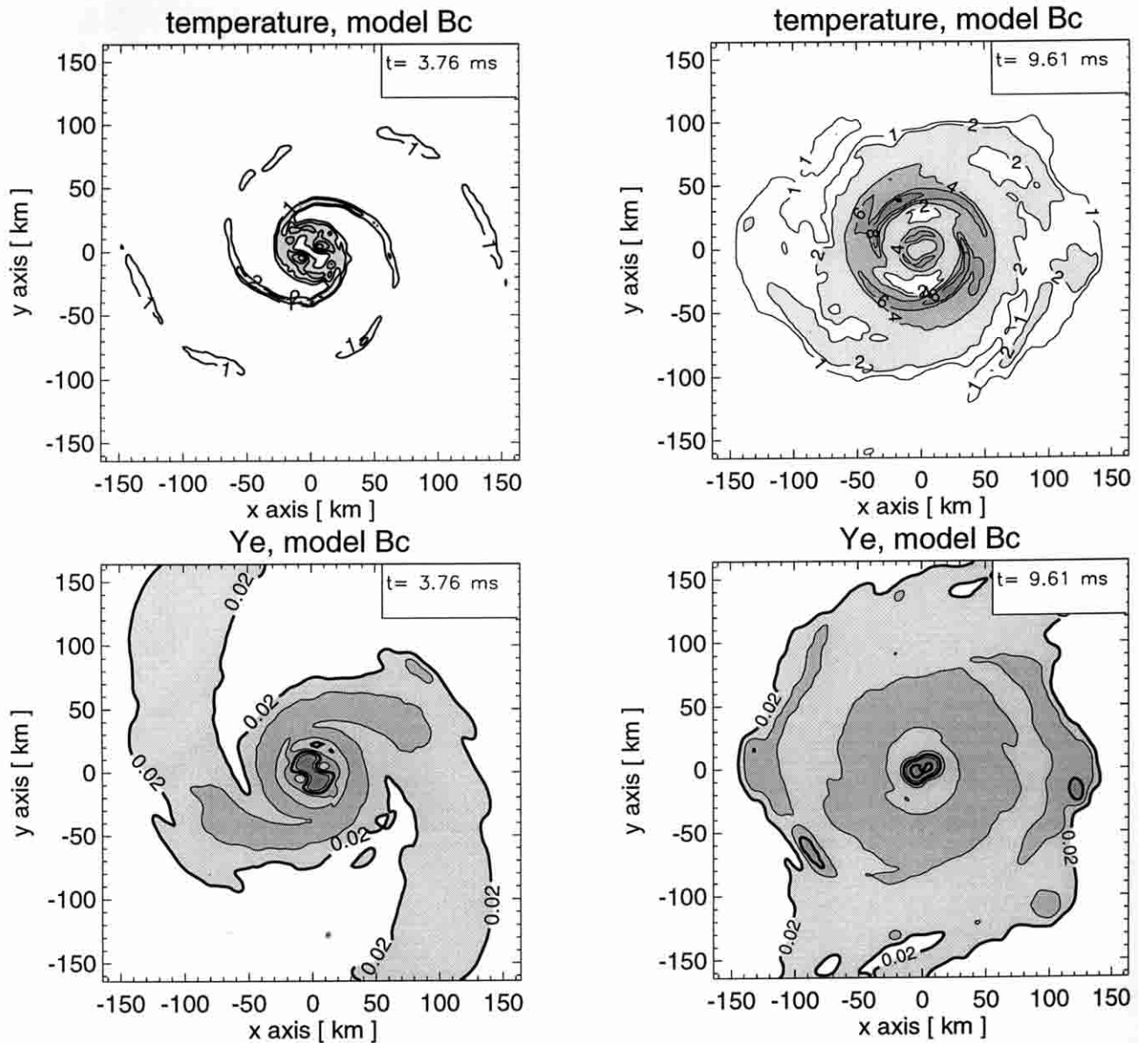
Fig. 16. Temperature and electron fraction in the orbital plane of Model B64c for two different times. In this model the entropy equation was used to follow the temperature evolution. The temperature contours are spaced linearly with levels at 1, 2, 4, 6, 8 and 10 MeV, the Y_e contours are given in steps of 0.02, starting with a value of 0.02. The plots should be compared with the corresponding panels in Figs. 3 and 14.

stars merge, and later during the numerous revolutions of the rapidly spinning central core within the surrounding layer of gas.

Most of the neutrino emission comes from the outer regions of dilute gas, because the dense core of the remnant is much less transparent to neutrinos. For this reason, the luminosities and mean energies of the emitted neutrinos and antineutrinos of all flavors are rather similar for Models B64 and B64c (Fig. 17), in particular towards the end of the simulations, when the extended gas cloud has reached a quasi-steady state. Before the tidal arms expand and shock heating and viscous shear has raised the temperatures in the outer parts of the merged stars, the neutrino emission of the initially cold Model B64c in fact

stays on a relatively low level ($\sim 10^{52}\,\mathrm{erg\,s^{-1}}$). During this phase the mean energies of the emitted neutrinos show large fluctuations.

The similarity of the neutrino production in the late phase of Models B64 and B64c is also visible in Fig. 18, where the total loss rates of neutrino energy per unit volume are displayed for both models. One can see that the dominant contribution to the emission of neutrinos of all flavors stems from the outer parts of the merger remnant and not from the very dense core. In both models, the location of the neutrinospheres, defined where the optical depth perpendicular to the orbital plane (i.e., effectively the minimum in all three coordinate directions of the cartesian grid) drops below unity (Eq. (7) in
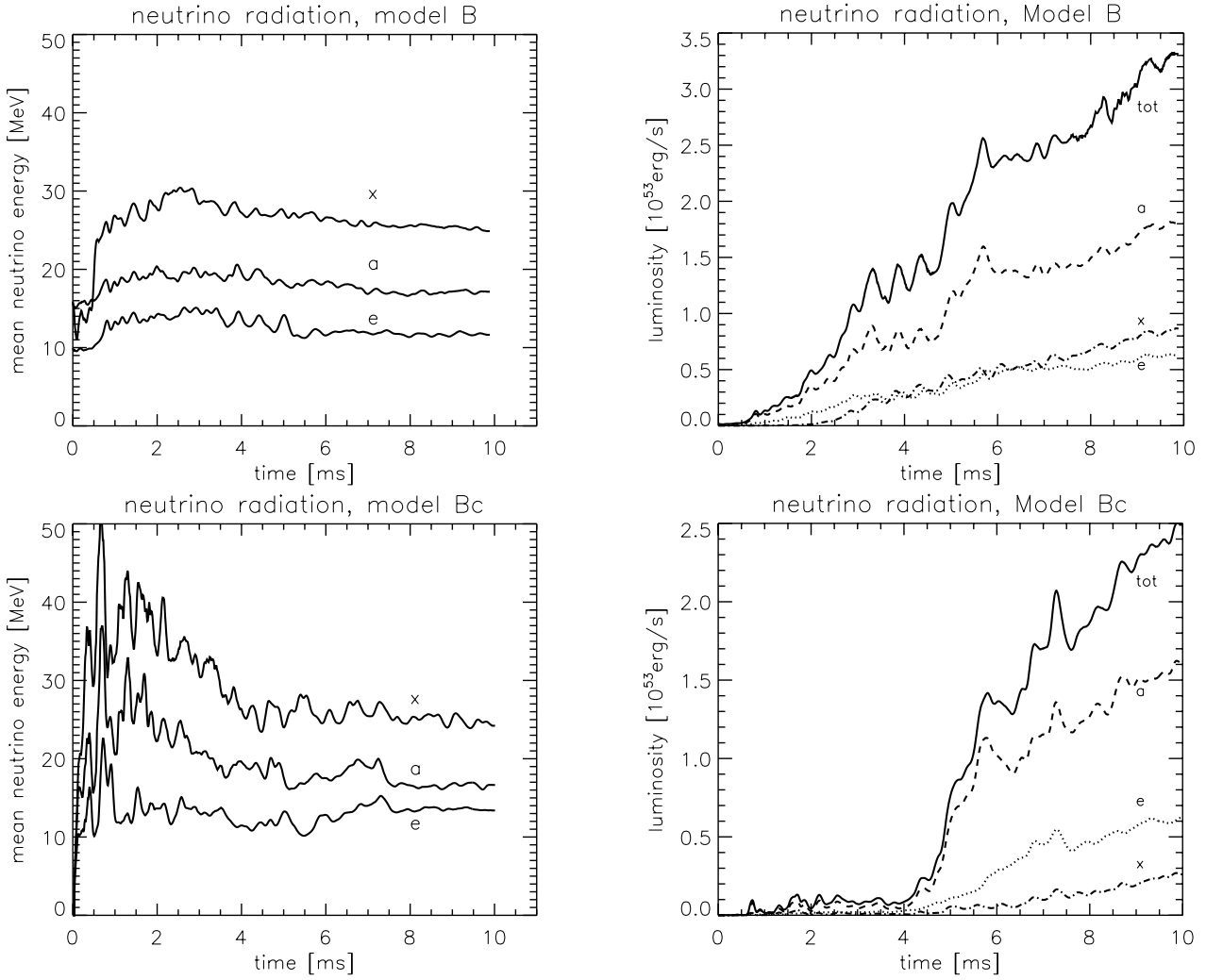
Fig. 17. Mean energies (left) and luminosities (right) of ν_e (label "e"), $\bar{\nu}_e$ (label "a") and heavy-lepton neutrinos and antineutrinos, ν_x (label "x"), as functions of time for Models B64 (top) and B64c (bottom). The luminosity of ν_x includes contributions from muon and tau neutrinos and antineutrinos.

Ruffert & Janka 1999), is also very similar. In the orbital plane the neutrinosphere radius is around 60–70 km. Perpendicular to the equator the density gradient is very steep and the neutrinospheres reach up to a vertical distance of about 20 km. The neutrinospheres of electron neutrinos (ν_e), electron antineutrinos ($\bar{\nu}_e$) and of the heavy-lepton neutrinos (μ and τ neutrinos and antineutrinos, ν_x, are produced with the same rates and "see" essentially the same opacity) are very close to each other. The neutrinosphere of ν_x is slightly smaller because there is no contribution of charged-current neutrino-nucleon interactions to the ν_x opacity.

The typical total neutrino luminosities at the end of the computed evolution are of the order of a few times $10^{53}\,\mathrm{erg\,s^{-1}}$ (Fig. 19). Within about 10 ms the models radiate an energy equivalent of roughly $10^{-3}\,M_\odot$ in neutrinos, which is more than an order of magnitude less than in gravitational waves (compare Figs. 19 and 11). These neutrino luminosities and energies are considerably larger than those given by Ruffert et al. (1997a) for comparable

models. The reason for this result is the use of the much larger grid in the current simulations. The previous models suffered from the problem that a significant amount of matter left the computational volume when the tidal tails expanded. In the present calculations this gas is wrapped up to form the shock-heated envelope around the dense core. Note that the position of the neutrinospheres is therefore *outside* of the computational volume that was employed by Ruffert et al. (1997a).

The largest contribution to the neutrino emission comes from electron antineutrinos, because positron captures on free neutrons dominate electron captures on protons. In the decompressed and hot neutron star matter, which forms the envelope around the merger core, neutrons are very abundant and the electron degeneracy is moderate, for which reason electron-positron pairs are present in large numbers. Because μ and τ neutrinos and antineutrinos are produced only by pair reactions (mainly $e^- + e^+ \rightarrow \nu + \bar{\nu}$) – but not by electron/position captures on protons/neutrons, which are the dominant processes
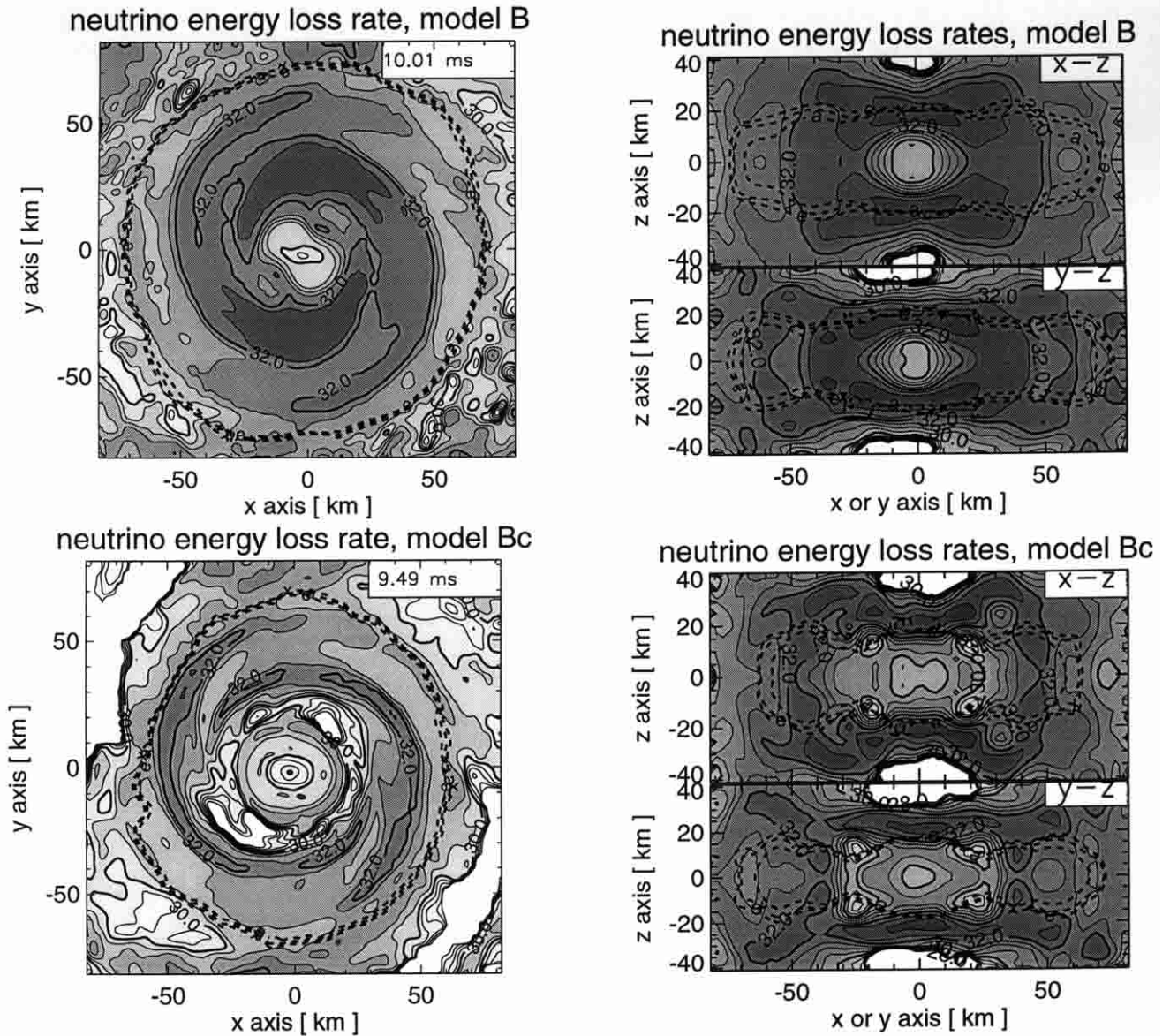
Fig. 18. Total neutrino energy loss rates (in $\mathrm{erg\,cm^{-3}\,s^{-1}}$) from the matter in the orbital plane and perpendicular to the orbital plane for Model B64 (top) and Model B64c (bottom) at the end of the computed evolution. The plots show the central region of the computational grid with the neutrinospheres of ν_x, $\bar{\nu}_\mathrm{e}$, and ν_e marked by dashed lines (in this order from inside outward). The contours are spaced logarithmically in steps of 0.5 dex.

for generating ν_e and $\bar{\nu}_\mathrm{e}$, respectively – their emission is extremely sensitive to the temperature (the energy production rate scales with T^9). Only in very hot models do they contribute to the neutrino emission on a significant level. For example, the difference of the total neutrino luminosities of Models B64 and B64c is almost entirely due to the emission of heavy-lepton neutrinos; the final luminosities of electron neutrinos and antineutrinos are essentially the same in both models (Fig. 19). The typical mean energies are around 11–13 MeV for the radiated ν_e, 15–19 MeV for $\bar{\nu}_\mathrm{e}$, and 22–27 MeV for ν_x (Table 2).

Figure 20 gives the energy loss rates per unit volume in the orbital plane of Model B64 at the end of the simulated evolution for all neutrino types (ν_e, $\bar{\nu}_\mathrm{e}$, and ν_x) individually and for the sum of all contributions. The orbital plane

is shown out to the boundaries of the computational grid. Although the three neutrinospheres nearly coincide, one notices clear differences of the spatial distribution of regions where the different types of neutrinos are produced. While ν_e are rather uniformly emitted from most of the matter, there are definite hot spots which radiate large amounts of $\bar{\nu}_\mathrm{e}$ and ν_x. This emphasizes the temperature sensitivity of the corresponding neutrino production processes, which require the presence of positrons in the stellar medium.

We evaluated two of our models, A64 and B64, for the energy deposition by the annihilation of neutrinos and antineutrinos to electron-positron pairs, $\nu + \bar{\nu} \rightarrow \mathrm{e}^- + \mathrm{e}^+$, as described by Ruffert et al. (1997a) and Ruffert & Janka (1999). The results at the end of the computed evolution
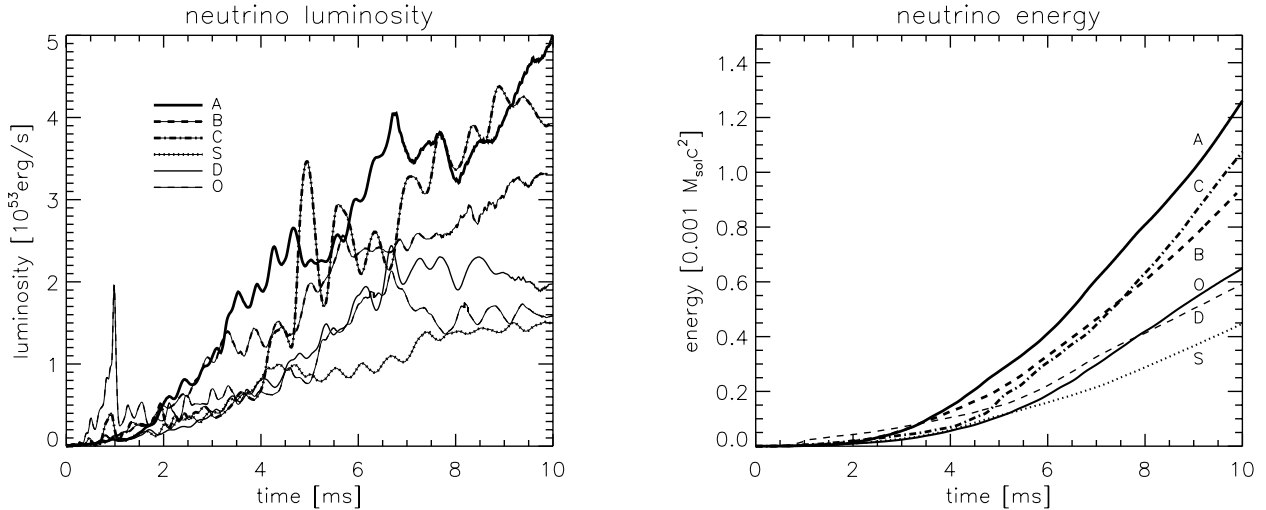
Fig. 19. Total neutrino luminosity (summed up for all flavors) and cumulative energy emitted in neutrinos as functions of time for different models.

(where the neutrino luminosities are highest) are plotted in Fig. 21. The largest energy deposition rates per unit volume are found above the poles of the merger remnant with peak values in excess of $10^{32}\,\mathrm{erg\,cm^{-3}\,s^{-1}}$. The numbers for the total rate of energy deposition in the volume where the gas density is below $10^{11}\,\mathrm{g\,cm^{-3}}$ are about $9 \times 10^{51}\,\mathrm{erg\,s^{-1}}$ in case of Model A64 and $7 \times 10^{51}\,\mathrm{erg\,s^{-1}}$ for Model B64 (Table 2). These rates are more than 20–30 times bigger than calculated by Ruffert et al. (1997a). This is mainly explained by the much higher neutrino luminosities in our current simulations, which enter the annihilation rate quadratically. (To some degree the effect is also caused by the different geometry, compare Fig. 21 with Fig. 16 in Ruffert et al. 1997a.)

The largest and by far dominant part of the energy deposition occurs in the polar regions. Here, however, also the energy loss rates by neutrino emission reach maxima (see the panels in the right column of Fig. 18), because high temperatures are present in a region where the gas is still dense, but the density gradient is very steep (Fig. 7). Therefore neutrinos are generated in large numbers and can easily escape to the transparent regime, as suggested by the fact that the neutrinospheres cross the regions of peak emission above the poles of the compact core (Fig. 18). With values up to more than $10^{33}\,\mathrm{erg\,cm^{-3}\,s^{-1}}$, the rate of energy loss exceeds the energy input rate by $\nu\bar{\nu}$ annihilation by more than a factor of about 10. Therefore the energy which is transferred to the stellar plasma will efficiently and immediately be reradiated by neutrino production processes, and the numbers for the total energy deposition rate in Table 2 overestimate the net heating effect by a large factor. The conclusion drawn by Ruffert et al. (1997a) and Janka & Ruffert (1996) remains valid: the energy deposited by neutrino-antineutrino annihilation in the neutrino-transparent, low-density plasma before, during, and immediately after the merging of two

neutron stars is not sufficient to explain the energetics of typical gamma-ray bursts.

4.4. Black hole formation and accretion

While the emission of gravitational waves peaks right at the moment when the two neutron stars fall into each other, the neutrino luminosity does not reach a very high level before the tidal tails have been inflated and wrapped up to the hot gas cloud that finally surrounds the dense core. Even then, neutrino-antineutrino annihilation is not an efficient mechanism to provide the energy for a gamma-ray burst, because electron and positron captures on free nucleons extract the deposited energy extremely rapidly from the dense gas that is present also above the poles of the merger remnant.

The situation changes, when the core of the remnant collapses to a black hole. Our basically Newtonian simulations, however, do not yield evidence whether and if so, when such a collapse occurs. Assuming that it happens, Ruffert & Janka (1999) continued the simulation of Model B64 for several ms to investigate the effects on the surrounding gas cloud. The black hole was represented by a gravitating "vacuum sphere", and the time of the gravitational instability was treated as a free parameter. The results for the dynamical evolution and the neutrino emission, however, turned out to be rather similar, independent of whether the black hole was assumed to form only $\sim 2\,\mathrm{ms}$ or as late as $10\,\mathrm{ms}$ after the start of Model B64.

A comparison of Fig. 15 in Ruffert & Janka (1999) with Fig. 7 in the present paper reveals that the baryonic matter above the poles of the compact core falls into the newly formed black hole very quickly. Within milliseconds, a funnel along the rotation axis is cleaned from baryons, and the density decreases to a value near our numerical lower limit of the density. With most of the energy deposition by neutrino-antineutrino annihilation taking place
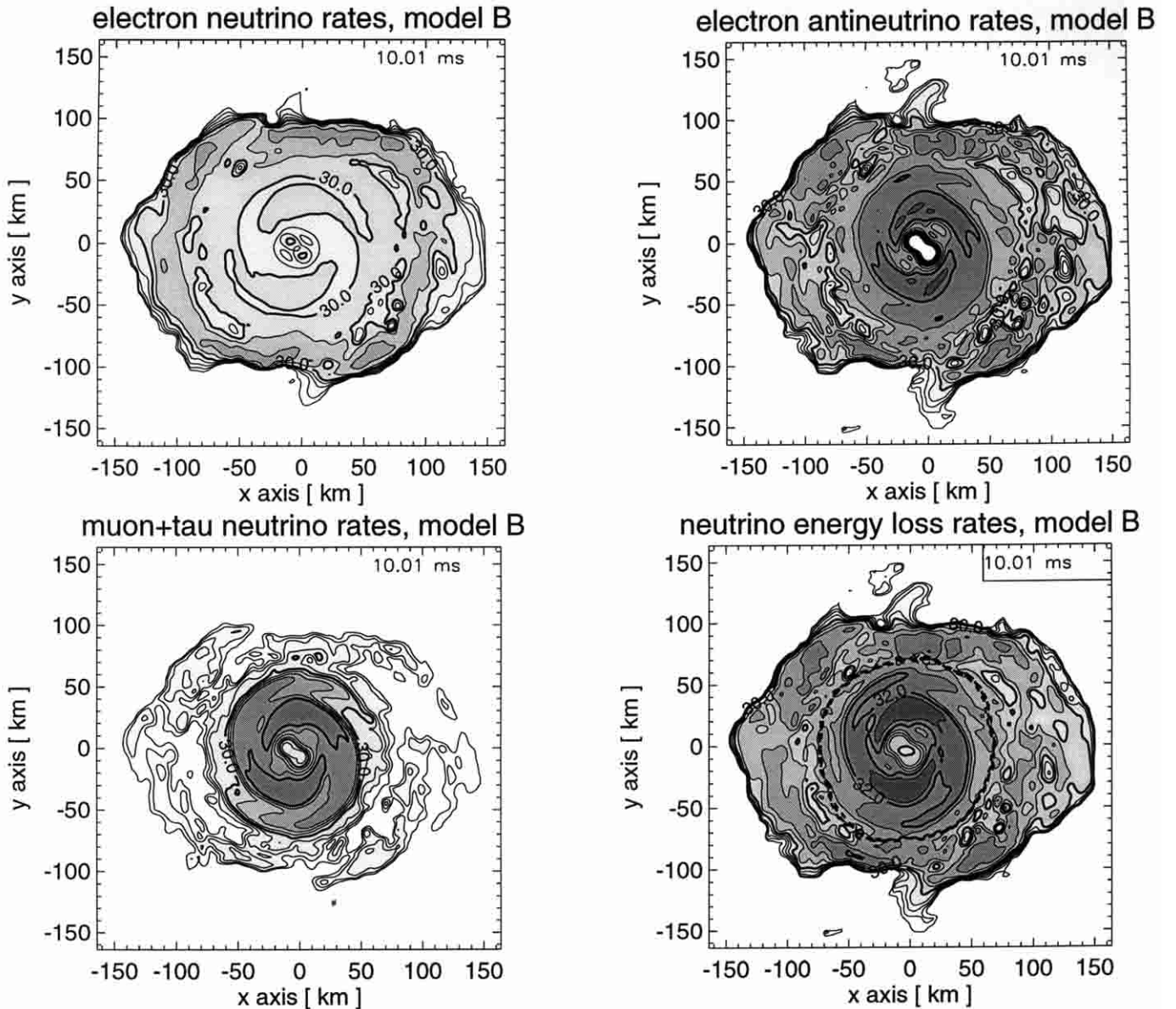
Fig. 20. Neutrino energy loss rates (in $\mathrm{erg\,cm^{-3}\,s^{-1}}$) from the matter in the orbital plane of Model B64 at the end of the computed evolution. The rates for ν_e (top left), $\bar{\nu}_e$ (top right), the sum of muon and tau neutrinos and antineutrinos (bottom left) and for neutrinos and antineutrinos of all flavors are given logarithmically, with steps of 0.5 dex. The dashed lines in the last plot indicate the positions of the neutrinospheres in the orbital plane.

in that region, this appears to be a favorable situation for a baryon-poor, potentially relativistic outflow to develop, which might later on produce a gamma-ray burst through dissipation of the mechanical kinetic energy into radiation.

Besides the formation of the black hole, such a scenario requires that a significant amount of matter remains in a disk around the black hole. The accretion of this matter on a timescale much longer than the dynamical timescale allows for a high efficiency of the conversion of rest-mass energy of the accreted gas to neutrinos. Typically several per cent efficiency in case of a Schwarzschild black hole and up to several ten per cent are possible for a Kerr black hole which accretes matter from a corotating (thin) disk (Thorne 1974; Shapiro & Teukolsky 1983;

Popham et al. 1999; Li & Paczyński 2000). Even more energy is available when the rotational energy of the black hole is tapped by means of magnetic fields (Blandford & Znajek 1977; Li 2000; Lee et al. 2000).

If a black hole forms from most of the mass of the merger remnant, our hydrodynamical models allow us to estimate the mass which ends up in an accretion disk around this black hole. Assuming that the disk is supported mainly by centrifugal forces, we use the criterion that the specific angular momentum of the gas should be larger than the Keplerian angular momentum at three Schwarzschild radii, i.e., at the location of the innermost stable circular orbit for a nonrotating black hole: $j > \sqrt{6}GM/c$, where M is taken to be the total mass on
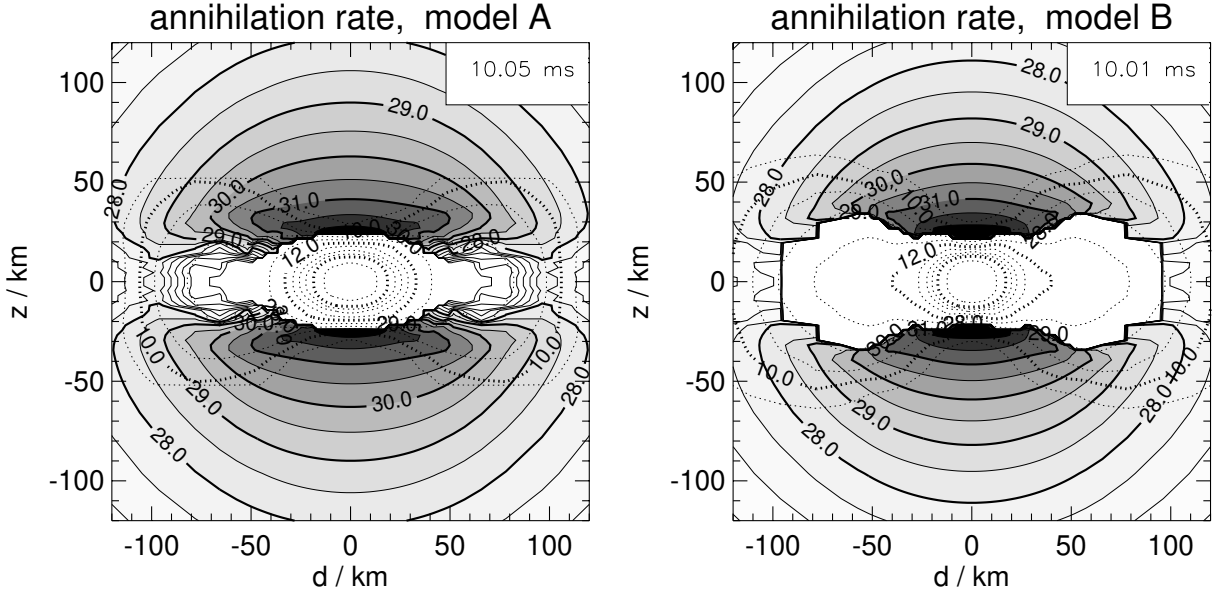
Fig. 21. Energy deposition rate (in $\mathrm{erg\,s^{-1}cm^{-3}}$) by the annihilation of neutrinos and antineutrinos to electron-positron pairs in the surroundings of the merger remnant for Models A64 (left) and B64 at the end of the computed evolution. Azimuthally averaged rates are shown in a plane perpendicular to the orbital plane. The corresponding solid contours are spaced logarithmically in steps of 0.5 dex. The dotted lines indicate the (azimuthally averaged) isodensity levels, also spaced logarithmically with steps of 0.5 dex. The rates are evaluated only in regions where the density is less than $10^{11}\,\mathrm{g\,cm^{-3}}$.
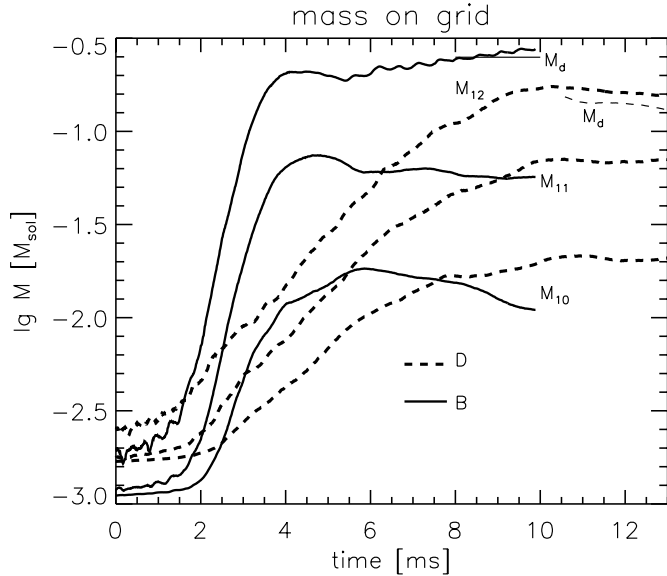

Fig. 22. Masses on the grid with a density below $10^{10}\,\mathrm{g\,cm^{-3}}$ ("M_{10}"), below $10^{11}\,\mathrm{g\,cm^{-3}}$ ("M_{11}"), and below $10^{12}\,\mathrm{g\,cm^{-3}}$ ("M_{12}"), respectively, for Models B64 (solid lines) and D64 (dashed lines) as functions of time. The thin curves mark the estimated disk masses, M_{d}, which encompass all gas with a specific angular momentum larger than the Keplerian angular momentum at three Schwarzschild radii of the merger remnant (i.e., of the total mass on the grid).

the grid. The corresponding gas masses, M_{d}, at the end of our simulations are listed in Table 1, and are indicated for Models B64 and D64 in Fig. 22. Typically, several hundredths of a solar mass up to a few tenths of a solar mass fulfill this condition. The largest numbers are obtained for

corotating models (B, S, D), where the gas has the highest specific angular momentum. The continuation of the simulation of Model B64 by Ruffert & Janka (1999) confirmed that these estimates are in reasonably good agreement with the gas mass which finally orbits around the black hole when a quasi-stationary state is reached.

For the irrotational A-case (and in the cases where the neutron stars started out with opposite spin directions or spins in counterrotation to the orbit), only a few per cent of the total rest mass of the binary system can gather enough angular momentum by hydrodynamical processes to be able to stay in a disk around a black hole at the end of our ~10 ms of computed evolution. These estimates are confirmed by three-dimensional simulations of neutron star mergers in full general relativity (Shibata & Uryū 2000, 2001). Of course, if the collapse to a black hole occurs immediately after the merging of the two neutron stars, before the tidal tails and the extended envelope of the merger remnant have a chance to form, there is no time for any transport of angular momentum by hydrodynamic interaction, and very little gas, if any at all, will be able to remain in a disk.

On grounds of our current hydrodynamical simulations, solving the time-dependent Euler equations, we cannot draw conclusions on the further development of the accretion "disk" or, better, of the extended torus. Once the gas has settled into a quasi-steady state around the newly-formed black hole, its later destiny will be driven by the radial transport of angular momentum, which is mediated by viscous forces, and the torus structure and internal conditions will be determined by the energy (and lepton) number loss through neutrino emission. Magnetic

fields can play an important role, too. In our simulations, without taking into account the effects of the physical disk viscosity (the numerical value of which cannot be determined from first principles and thus would have to be considered as a free parameter within the Navier-Stokes equations), the subsequent evolution is governed by the action of the numerical viscosity, which is not under our direct control, but can be varied only indirectly by changing the grid resolution. In addition, numerical viscosity does not have the same properties as the physical viscosity, e.g., it does not necessarily conserve the angular momentum.

Considering the situation at the end of our models we therefore could only speculate about the long-time evolution of the accretion torus (Ruffert & Janka 1999; Janka et al. 1999). With a given value for the mass accretion rate by the black hole, for example, we obtained an estimate of the torus lifetime. Moreover, the mass, density, and temperature of the torus define its neutrino emission properties, and the calculated neutrino luminosity (extrapolated for the estimated accretion time) allows one to come up with numbers for the efficiencies of conversion of gravitational potential energy to neutrinos and to the electron-positron pair plasma by neutrino-antineutrino annihilation.

Typical temperatures within the torus are a few MeV, the maximum temperatures between about 5 MeV and roughly 10 MeV. A significant amount, if not most of the torus mass has a density above $10^{11}\,\mathrm{g\,cm^{-3}}$ (Fig. 22 and Table 2). "Massive" tori, i.e., those with a mass of more than $\sim 0.1\,M_\odot$, are optically thick to neutrinos, whereas tori with masses of only a few $0.01\,M_\odot$ are close to neutrino transparency (see Fig. 30 in Ruffert & Janka 1999).

Whether the dense core of the merger remnant collapses to a black hole, and if so, on what timescale this happens, is a complex question, which requires not only a general relativistic treatment, but depends on a number of additional aspects, e.g., the mass and compactness of the initial neutron stars, the properties of the nuclear EoS, and the rotation of the post-merging object. Shibata & Uryū (2000, 2001), by performing three-dimensional dynamical simulations in full general relativity, find that the product of a neutron star merger is sensitive to the initial compactness of the neutron stars, which is defined as the ratio of the Schwarzschild radius of the neutron star to its actual radius. This quantity increases when the mass of the neutron star approaches the limiting mass of a spherical star in isolation. For sufficiently compact stars a black hole is formed on a dynamical timescale, as the compactness descreases, the formation timescale becomes longer and longer. (The corresponding critical mass of the binary relative to the mass limit of a nonrotating, single neutron star varies with the compressibility of the EoS.) For less compact cases, a differentially rotating "supramassive" neutron star (Cook et al. 1992, 1994a,b) forms, which first has to become a rigidly rotating body (on a secular timescale by viscous dissipation) or has to lose some of its angular momentum by dynamical processes (e.g., mass stripping, bar-mode instability) or secular
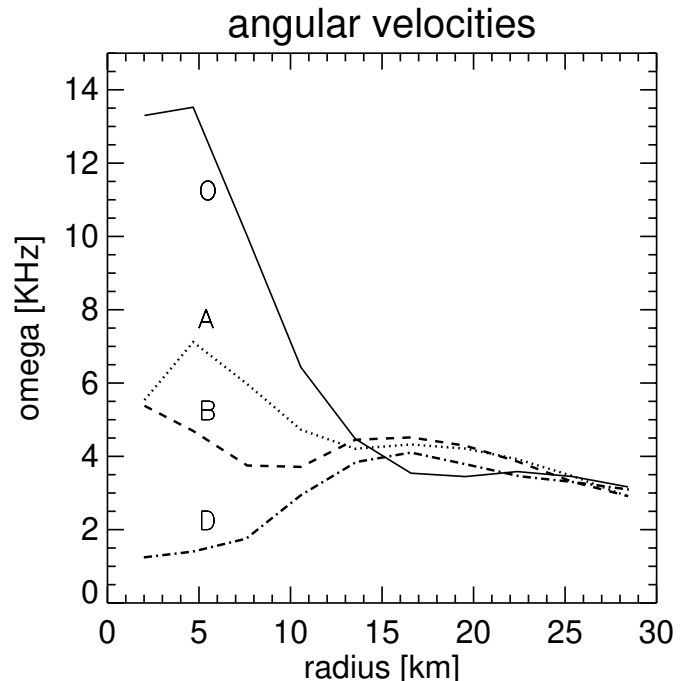

Fig. 23. Azimuthally averaged angular velocity in the orbital plane as a function of the distance from the system axis. The plot shows the inner regions of the merger remnants of Models A64, B64, O64, and D64 at the end of the computed evolution.

processes (e.g., gravitational waves, mass loss by winds, magnetic fields), before the gravitational instability can set in (Shibata et al. 2000).

Thus the evolution leads to a black hole very quickly only if the total rest mass of the binary system is sufficiently larger than the maximum rest mass of a spherical star in isolation. The exact factor depends on the stiffness of the EoS as well as on the angular momentum of the binary system. The latter determines the rotation of the core of the merger remnant, which can remain stable although it has a mass that is significantly larger than the mass limit of spherical or rigidly rotating neutron stars because of the supporting effect of rapid, differential rotation (Baumgarte et al. 2000).

Our models have a dimensionless rotation parameter $a \equiv Jc/(GM^2)$ (J is the total angular momentum, M the total rest mass of the system), which initially is between 0.64 for Model C64 and 0.98 for Model S64. During the evolution, the mass changes only slightly, because little gas escapes from the system. In contrast, the angular momentum decreases significantly due to the emission of gravitational waves (and partly due to angular momentum which is carried away by the ejected gas). The final values of the parameter a are therefore lower, between about 0.5 for Model C64 and 0.75 for Model S64 (see the columns a_i and a_f in Table 2 of Janka et al. 1999; the actual numbers might be up to $\sim 10\%$ larger, because one should apply corrections for the numerical loss of angular momentum). This suggests that the merger remnant has an angular momentum below the critical limit that is possible for a

Kerr black hole ($a = 1$). Of course, a definite statement of this kind is not possible without a relativistic treatment, which considers M to be the gravitational mass instead of the rest mass, and includes the mass reducing effect of the energy loss by gravitational waves. The latter, however, is small. According to the quadrupole formula less than $\sim$1% of the mass of the system is emitted in gravitational waves (Fig. 11). Therefore the trend seen in our Newtonian calculations should be right, and the subcritical rotation of the merger remnant should even be quantitatively correct if one does not start with an initial value of a that is much larger than unity.

It is worth a final remark that the compact core of the merger remnant at its "surface" near 25 km rotates with an angular velocity that is only slightly lower than the Keplerian frequency, $\Omega_K = \sqrt{GM/r^3} \sim (4 \ldots 5) \times 10^3 \, \mathrm{s}^{-1}$. The degree of differential rotation, however, varies strongly between the different models and depends on the initial neutron star spins and the mass ratio of the neutron stars. Figure 23 shows the azimuthally averaged angular velocities in the orbital plane for the core of the remnant in different models at the end of the computed evolution. Whereas in the irrotational, symmetric case, Model A64, the core rotates moderately differentially with radially decreasing mean angular velocity, the asymmetric Model D64 reveals the opposite trend, and the corotating case, Model B64, is near rigid rotation. The most dramatic differential rotation is found in the inner region of Model O64, where the mean angular velocity drops from roughly $14 \times 10^3 \, \mathrm{s}^{-1}$ near the center to a value around $3.5 \times 10^3 \, \mathrm{s}^{-1}$ between 15 km and 30 km distance from the system axis. We would like to emphasize, however, that except for Model O64, the different grid zones at a fixed equatorial radius show large fluctuations of the corresponding value of Ω, because the merger remnants are still significantly perturbed and perform violent oscillations.

5. Summary, discussion, and conclusions

We have presented results of neutron star merger simulations that were performed with a new version of our numerical code, which was significantly improved compared to the original one (Ruffert et al. 1996, 1997a), mainly by the introduction of several levels of nested grids. These allow for a better resolution of the stars near the grid center on the one hand, and a larger computational volume on the other. Besides recomputing our previously published models with the new code, we varied the neutron star parameters (masses, mass ratios, spins) and computed models with different maximum resolution. The lower resolution on the finest grid was similar to the grid in our older calculations, whereas the current "standard models" have a factor of two higher resolution in all three cartesian directions. Moreover, we tested the accuracy (or uncertainty) of the temperature calculation by replacing the energy (i.e., the sum of kinetic and internal energies in our code) by the entropy as the basic variable to follow the temperature evolution in time.

Using the energy for deriving temperatures has the disadvantage that the thermal energy is only a small contribution to the internal energy. The latter is dominated by the degeneracy energy of the fermions. This leads to errors in the temperature determination when the internal energy is not very accurate. With the entropy equation one also reduces, although cannot eliminate, the problem that unphysical shocks at the interface between the neutron stars and the surrounding medium occur and cause an overestimation of the temperature, in particular before the merging. Even more, the entropy equation gives one control over the effects of shear and bulk viscosity on the thermal evolution, whereas the temperature calculated from the energy equation does not allow this direct control, because the dissipative effects of numerical viscosity in the code can be influenced only by changing the grid resolution. Of course, solving the entropy equation as a supplementary equation in addition to the conservation laws of mass, momentum, energy, and lepton number, which still describe the evolution of the stellar fluid (and where the neutrino source terms were evaluated with the temperature as obtained from the entropy equation), is not a hydrodynamically fully consistent approach. We therefore do not consider this procedure as the necessarily more accurate calculation, but as an attempt to test the sensitivity of our results to effects that are associated with the uncertainties of the temperature determination discussed above. It is reassuring that despite of significant differences of the thermal evolution our main results show rather little variation.

In fact, this work was also strongly motivated by the wish to investigate and outline (at least some) major uncertainties of (not only our) current neutron star merger simulations. Such uncertainties have a bearing on the possibility to draw model-based conclusions on the gravitational-wave emission, a potential connection with gamma-ray bursts, and the implications for the production of heavy elements in our Galaxy. The models presented in this paper improve our previous calculations with respect to numerical resolution and reduced mass loss through the outer boundaries of the significantly enlarged computational grid. They are intended to serve for comparisons with future general relativistic simulations.

5.1. Main results

In summary, our main results and their implications are the following. The details of the gravitational-wave signal, i.e., the primary and subsequent maxima of the luminosity, the total radiated energy, and the structure of the wave amplitude in particular during the post-merging phase, when the core of the merger remnant is in a highly perturbed state and performs violent oscillations, exhibit some change with the resolution on the finest grid. A cell size of 0.64 km or smaller, corresponding to at least 50 zones on the diameter of the initial neutron star, seems desirable. With less resolution, the effects of

numerical viscosity and the associated loss of angular momentum grow to an unacceptable level and characteristic features of the gravitational-wave emission are noticably influenced. This limits the possibility to deduce important information from a possible future wave measurement. The gravitational waves which accompany the final plunge of the neutron stars, carry information about the masses, compactness and the spins of the neutron stars and thus allow for conclusions on the nuclear EoS. The post-merging signal yields evidence about the destiny of the merger remnant and can also be used to extract information about the internal state of neutron stars.

While the gravitational-wave emission is strongest when the two neutron stars plunge into each other, the neutrino emission rises only gradually afterwards. It approaches a saturation level towards the end of our simulations, when the tidal tails have been wrapped up to a cloud of shock- (and shear-)heated gas that surrounds the compact and much denser core of the merger remnant. Because of the more extended computational grid, which is necessary to follow the development of this gas cloud, the neutrino luminosities are found to be a factor of 2–4 higher than in our previously published models (Ruffert et al. 1997a). Correspondingly, the energy deposition rates by neutrino-antineutrino annihilation in the dilute outer layers ($\rho \lesssim 10^{11}\,\mathrm{g\,cm^{-3}}$) of the post-merging object are up to a factor of 20–30 larger. By far the dominant part of this energy, however, is deposited in the polar regions, where the temperature is high and the scattering depth to neutrinos is rather low. Therefore this energy is immediately reradiated through neutrinos produced by electron and positron captures on nucleons. Such an energy transfer to a region with large baryon density is therefore inefficient in powering a gamma-ray burst, and should drive a baryonic wind rather than a relativistic outflow of a baryon-poor pair-photon plasma. This presumably high-entropy wind (i.e., the medium has low density but comparatively high temperature), which expands into vacuum, may have very interesting, so far not investigated, implications for observable radiation from neutron star merging events, and for the enrichment of our Galaxy with heavy elements (a more detailed discussion can be found in Ruffert & Janka 1999; Janka & Ruffert 2001).

The dynamical mass ejection from the merging binary varies with the initial spins of the neutron stars. It is largest ($\sim (2 \dots 4) \times 10^{-2}\,M_\odot$ or roughly 1% of the system mass) for corotating systems (a case which is not likely to be realized because of the small viscosity of neutron star matter, which cannot bring the system into a tidally locked state prior to merging; Kochanek 1992; Bildsten & Cutler 1992) and smallest ($\lesssim 10^{-4}\,M_\odot$) when the stars initially counterrotate with the orbit. Only in the former case very prominent tidal arms develop through the outer Lagrange points and expand away from the center of the merger. The use of the larger computational volume helped to significantly improve our estimates for the amount of mass which can potentially become unbound.

It is an important aim of numerical models to determine the thermodynamical conditions and the nuclear composition of these ejecta, and their subsequent evolution. This will help answer the question whether and how r-processing can take place in this matter (Lattimer & Schramm 1974, 1976; Symbalisty & Schramm 1982; Meyer 1989; Davies et al. 1994; Freiburghaus et al. 1999) and whether it has contributed to the heavy-element content of our Galaxy at a significant level.

We find that the matter, which is ejected from the tips of the expanding tidal tails, stays cool, because it is neither heated by shocks nor by viscous friction. In fact, it is a problem in hydrodynamical simulations to accurately trace the thermal history of the initially cold neutron matter (the viscosity is not only too small to achieve tidal locking, it is also too small to heat the neutron stars beyond $\sim 10^9$ K before merging; Lai 1994). Besides the high degeneracy of the medium, numerical viscosity, which is present to some (but actually different) degree in all numerical codes and depends on the resolution, causes problems for an accurate calculation of the temperature. In addition, the limited numerical resolution does not allow one to properly represent the extremely steep density gradient near the neutron star surface below a density of about $10^{14}\,\mathrm{g\,cm^{-3}}$. This leads to the necessity of softening the density gradient to produce (nearly) hydrostatic conditions. In our Eulerian, grid-based simulations the neutron stars also have to be embedded by a low-density medium. When the neutron stars move through this surrounding medium, shocks occur at the stellar surfaces in upstream direction, which produces artificial heating. Thus locally, the temperatures can be overestimated by a large factor, although this numerical heating is small compared to the maximum temperatures which are reached when the two neutron stars plunge into each other. Because of all these aspects, some of which are not specific to a particular code but are generic to the physical problem or to hydrodynamical simulations with limited resolution, the calculated temperatures are likely to be overestimated and have to be interpreted with special caution. Significant progress requires a much enlarged numerical resolution. For grid-based codes this could be achieved by employing adaptive mesh refinement techniques. Another option for improving some aspects may be the choice of a rotating instead of a fixed frame of reference (New & Tohline 1997; Swesty et al. 2000), although the inspiral is so rapid that there would quickly be motion of the stars also in a reference frame that is initially corotating.

Our merger simulations followed the variation of Y_e in response to electron captures by protons and positron captures by neutrons, including also the effects of neutrino trapping when the stellar medium becomes optically thick to neutrinos at sufficiently large densities. Although these weak interaction rates are fast at temperatures between 10^{10} K and 10^{11} K, they are not effective in raising the initial electron fraction on the very short timescale of the dynamical expansion of the ejecta. Starting with a typical equilibrium Y_e around 0.02 in the tidal tails, we cannot

find a growth by more than a factor of 2–3 (to values of at most ∼0.06) before the gas leaves our computational grid. At that time the density has decreased to $10^{10}\,\mathrm{g\,cm^{-3}}$ or less, and the matter has cooled down to $(2–3) \times 10^{10}\,\mathrm{K}$. Since both the temperature and the density drop quickly, and more and more nucleons recombine to alpha particles and nuclei, we do not expect a significant effect due to electron and positron captures during the subsequent expansion. This result was obtained although the temperature (and therefore the mass fraction of free nucleons) was overestimated in our simulations, implying unrealistically fast electron and positron captures on the free protons and neutrons. In comparative calculations, using the entropy equation for following the thermal history of the medium (see above) and starting with lower (and thus more realistic) temperatures, we actually cannot detect any change from the initial value of Y_e. We emphasize that our point here is the fact that neutrino processes seem to be unable to alter Y_e during the rapid decompression of essentially cold neutron star matter. The initial Y_e of the neutron star crust is therefore preserved, although the exact value may be EoS dependent and is therefore uncertain.

5.2. Elements of a possible r-process site

Cold material in neutron star crusts consists of neutron-saturated, very neutron-rich nuclei that are arranged on a lattice and immersed in a gas of neutrons and degenerate electrons (e.g., Weber 1999). This region has a very low proton-to-nucleon ratio ($Y_e \sim 0.02$; only in a thin skin layer of the neutron star, the outer crust, the electron fraction rises again). As discussed above, it is unlikely that the decompressed and expanding matter in the tidal tails is heated by dissipative processes (shocks, viscous shear) to temperatures where nuclear statistical equilibrium sets in ($T \gtrsim 5 \times 10^9$ K). Therefore the memory of the initial nuclear composition is not erased during this phase of the expansion, and the subsequent changes of the nuclear abundances have to be determined by following the beta-decays of the initial ensemble of heavy nuclei (Hilf et al. 1974; Lattimer et al. 1977; Meyer 1989). Since heating by beta-decays can raise the temperatures to several 10^9 K without, however, necessarily destroying the memory of the initial composition (Meyer 1989; Sumiyoshi et al. 1998), a self-consistent coupling of the hydrodynamical evolution with the effects of nuclear decays, including the decay heating and possible (γ, p) and (γ, n) reactions, is essential for reliable predictions of the final nucleosynthetic yields. Calculations fulfilling these conditions have not been performed so far, and it remains to be seen whether this scenario yields a solar system like distribution of r-process elements.

In contrast, Freiburghaus et al. (1999) assumed that the ejected gas starts from nuclear statistical equilibrium, i.e. with a temperature above ∼5 × 10⁹ K, because they used the EoS of Lattimer & Swesty (1991), which was actually developed for supernova conditions and does not

contain the physics required to describe cold neutron stars. Combining hydrodynamic results of neutron star merger simulations with network calculations, they found that for proton-to-nucleon ratios around 0.1 rapid neutron captures produce an abundance pattern which fits the observed solar r-process very well for nuclear masses around and above the $A \approx 130$ peak. However, they considered Y_e as a free parameter instead of determining it as a result of neutrino emission and absorption reactions in the hydrodynamical merger model. Moreover, the feedback of beta-decay heating on the hydrodynamic evolution of the fluid elements was not taken into account.

Based on our simulations we come to the conclusion that the ejected gas stays cool, does not get heated by shocks or viscous shear to temperatures where nuclear statistical equilibrium holds, and retains its very low initial proton-to-nucleon ratio. Therefore our simulations do not yield the conditions which were determined by Freiburghaus et al. (1999) as favorable for producing a solar-like r-process abundance pattern in the $A \gtrsim 130$ mass range. Our models do not provide evidence that their values for the initial temperature and composition are realised in the ejecta from neutron star mergers. Instead, our results seem to favor the kind of scenario discussed by Lattimer et al. (1977) and Meyer (1989), who considered the decompression of initially cold matter from the inner crust of neutron stars, where the composition is dominated by extremely neutron-rich nuclei (heavy metals) that can be arranged on a lattice and are immersed in a gas of neutrons and relativistic electrons. However, it is unclear whether the decompression from such an initial state leads to the abundance distribution of rapid neutron capture elements as observed in the solar system.

Besides beta-decays, electron and positron captures and (γ, p) and (γ, n) reactions, a detailed discussion of the nucleosynthesis in the dynamically ejected matter might also require taking into account the interaction with the intense fluxes of energetic neutrinos from the merger remnant. Neutrinos absorbed by nucleons and scattered by nuclei in the outflowing gas may heat and accelerate the gas, may change the proton-to-neutron ratio and may reprocess the heavy elements by inducing nuclear transmutations. Although the neutrino emission from the remnant rises only gradually after the tidal tails have formed, and the timescale of the expansion of the gas away from the merger site is very short (of the order of the escape timescale, which is roughly $t_{\mathrm{exp}} \sim r/v_{\mathrm{esc}} \sim 1\,\mathrm{ms}$), the number of neutrino-nucleon interactions can be estimated to be significant. An order of magnitude evaluation shows that about 10% of the nucleons might react with neutrinos:

$$\int_{R_i}^{\infty} \mathrm{d}r\, \frac{\mathcal{R}}{n_b v(r)} \sim 0.1\, \alpha\, \langle \epsilon_\nu \rangle_{20}\, L_{\nu,53}\, (M_3\, R_{i,7})^{-1/2}, \quad (11)$$

where $\mathcal{R}$ is the reaction rate per neutrino per unit of volume, $\langle \epsilon_\nu \rangle_{20}$ the mean energy of the emitted neutrinos measured in 20 MeV, $L_{\nu,53}$ the total neutrino luminosity in $10^{53}\,\mathrm{erg\,s^{-1}}$, M_3 the mass of the remnant normalized

to $3\,M_\odot$, and $R_{i,7}$ the initial radius in units of $10^7\,$cm. The radial velocity was assumed to be roughly given by $v(r) = \sqrt{2GM/r}$, and the neutrino interaction cross section was approximated by the absorption cross section of ν_e and $\bar{\nu}_e$ on nucleons, $\sigma \sim 10^{-43}(\epsilon_\nu/1\,\text{MeV})^2\,\text{cm}^2$, because electron neutrinos and antineutrinos dominate the neutrino emission of the merger remnant. The quantity α is a geometrical factor and is less than unity. It accounts for the fact that the neutrinos are radiated mainly perpendicular to the orbital plane (because in this direction the scattering depth is smaller), whereas the dynamically ejected gas moves away from the system in the plane of the binary orbit.

The amount of dynamically ejected material varies strongly with the neutron star spins and is largest for the improbable case of corotating systems. Moreover, it is sensitive to the stiffness of the unknown nuclear EoS (Freiburghaus et al. 1999; Rosswog et al. 2000). Because momentum has to be transferred by hydrodynamical processes before gas can be expelled, mass ejection may even be suppressed by a quick collapse of the merger remnant to a black hole, a possibility which depends on the neutron star equation of state, the masses of the merging stars, and the angular momentum of the binary system (Shibata & Uryū 2001). In view of these fundamental uncertainties, current models are unable to yield quantitatively meaningful numbers for the contribution of neutron star mergers to the metal enrichment of our Galaxy, even if the theoretical estimates of the merger rates were reliable (which in fact is not the case).

5.3. Concluding remarks

We have presented results from state-of-the-art simulations of neutron star mergings with the most advanced version of our hydrodynamics code, and have discussed these results and their limitations. Of course, our calculations are far from being satisfactory. Relativistic simulations are necessary to address the question whether a black hole forms and if so, on what timescale it happens. This is important not only for predictions of the gravitational-wave signal and the mass which can become unbound during the merging. It is also important for studying the implications of neutron star mergers for the origin of heavy elements and has consequences for potentially observable signals connected with the neutrino- and photon-cooling phases of the remnant, which is either a rotating (supramassive), hot neutron star or a black hole which accretes matter from a surrounding torus at very high rates.

So far our treatment of neutrino production and emission by using a trapping scheme does not allow us to study the effects of neutrino transport and neutrino energy deposition in the outer layers of the merger remnant. The latter should drive a baryonic outflow from the massive neutron star or from the accretion disk around the black hole. Including the feedback of neutrino interactions is essential for modeling this mass loss and for determining the conditions in the wind.

This discussion shows that the modeling of the merging of neutron stars and of the accompanying physical processes is still at its beginning. Current simulations do neither fully account for the effects of general relativity, nor do they include all the physics which is relevant to come up with meaningful predictions of the potentially observable photon and neutrino emission, or to clarify the role of neutron star mergers for the production of heavy elements in our Galaxy. Therefore conclusions drawn from current hydrodynamical models have to be considered with special reservation. We have outlined a number of aspects where improvements and progress in future simulations are highly desirable.

References

Akmal, A., Pandharipande, V. R., & Ravenhall, D. G. 1998, Phys. Rev. C, 58, 1804

Ayal, S., Piran, T., Oechslin, R., Davies, M. B., & Rosswog, S. 2001, ApJ, 550, 846

Baumgarte, T. W. 2001, in Astrophysical Sources of Gravitational Radiation, ed. J. M. Centrella (AIP Press), in press [gr-qc/0101045]

Baumgarte, T. W., Shapiro, S. L., & Shibata, M. 2000, ApJ, 528, L29

Baumgarte, T. W., Cook, G. B., Scheel, M. A., Shapiro, S. L., & Teukolsky, S. A. 1998a, Phys. Rev. D, 57, 6181

Baumgarte, T. W., Cook, G. B., Scheel, M. A., Shapiro, S. L., & Teukolsky, S. A. 1998b, Phys. Rev. D, 57, 7299

Bildsten, L., & Cutler, C. 1992, ApJ, 400, 175

Blanchet, L., Damour, T., & Schäfer, G. 1990, MNRAS, 242, 289

Blandford, R. D., & Znajek, R. L. 1977, MNRAS, 179, 433

Bonazzola, S., Gourgoulhon, E., & Marck, J.-A. 1999, Phys. Rev. Lett., 82, 892

Bulik, T., Belczynski, K., & Zbijewski, W. 1999, MNRAS, 309, 629

Centrella, J. M., & McMillan, S. L. W. 1993, ApJ, 416, 719

Colella, P., & Woodward, P. R. 1984, J. Comput. Phys., 54, 174

Cook, G., Shapiro, S. L., & Teukolsky, S. A. 1992, ApJ, 398, 203

Cook, G., Shapiro, S. L., & Teukolsky, S. A. 1994a, ApJ, 422, 227

Cook, G., Shapiro, S. L., & Teukolsky, S. A. 1994b, ApJ, 424, 823

Cooperstein, J. 1988, Phys. Rep., 163, 94

Cutler, C., & Flanagan, E. E. 1994, Phys. Rev. D, 49, 2658

Davies, M. B., Benz, W., Piran, T., & Thielemann, F. K. 1994, ApJ, 431, 742

Duncan, R. C., Shapiro, S. L., & Wasserman, I. 1986, ApJ, 309, 141

Eichler, D., Livio, M., Piran, T., & Schramm, D. N. 1989, Nature, 340, 126

Faber, J. A., & Rasio, F. A. 2000, Phys. Rev. D, 62, 064012

Faber, J. A., Rasio, F. A., & Manor, J. B. 2001, Phys. Rev. D, 63, 044012

Flanagan, E. E. 1999, Phys. Rev. Lett., 82, 1354

Freiburghaus, C., Rosswog, S., & Thielemann, F.-K. 1999, ApJ, 525, L121

Fryer, C. L., Woosley, S. E., & Hartmann, D. 1999, ApJ, 526, 152

Haensel, P., & Schaeffer, R. 1992, Phys. Rev. D, 45, 4708

Heiselberg, H., & Pandharipande, V. 2000, Ann. Rev. Nucl. Part. Sci., 50, 481

Hilf, E. R., Hillebrandt, W., Takahashi, K., El Eid, M. F., & Kodama, T. 1974, Phys. Scrip., 10A, 132

Hulse, R. A., & Taylor, J. H. 1975, ApJ, 195, L51

Janka, H.-T., & Ruffert, M. 1996, A&A, 307, L33

Janka, H.-T., & Ruffert, M. 2001, in Proc. Conf. on Stellar Collisions and Mergers, ed. M., Shara, ASP Conf. Ser., in press [astro-ph/0101357]

Janka, H.-T., Eberl, T., Ruffert, M., & Fryer, C. L. 1999, ApJ, 527, L39

Kalogera, V., & Lorimer, D. R. 2000, ApJ, 530, 890

Kochanek, C. S. 1992, ApJ, 398, 234

Lai, D. 1994, MNRAS, 270, 611

Lai, D., & Shapiro, S. L. 1995, ApJ, 443, 705

Lai, D., & Wiseman, A. G. 1996, Phys. Rev. D, 54, 3958

Lai, D., Rasio, F. A., & Shapiro, S. L. 1994a, ApJ, 420, 811

Lai, D., Rasio, F. A., & Shapiro, S. L. 1994b, ApJ, 423, 344

Landau, L. D., & Lifschitz, E. M. 1991, Lehrbuch der Theoretischen Physik, Band VI (Hydrodynamik, 5. Auflage) (Akademie Verlag, Berlin)

Lattimer, J. M., & Schramm, D. N. 1974, ApJ, 192, L145

Lattimer, J. M., & Schramm, D. N. 1976, ApJ, 210, 549

Lattimer, J. M., & Swesty, F. D. 1991, Nucl. Phys. A, 535, 331

Lattimer, J. M., Mackie, F., Ravenhall, D. G., & Schramm, D. N. 1977, ApJ, 213, 225

Lee, H. K., Wijers, R. A. M. J., & Brown, G. E. 2000, Phys. Rep., 325, 83

Li, L.-X. 2000, ApJ, 533, L115

Li, L.-X., & Paczyński B., 2000, ApJ, 534, L197

Lombardi, J. C., Rasio, F. A., & Shapiro, S. L. 1997, Phys. Rev. D, 56, 3416

Marronetti, P., Mathews, G. J., & Wilson, J. R. 1999, Phys. Rev. D, 60, 087301

Mészáros, P., & Rees, M. J. 1992, ApJ, 397, 570

Mészáros, P., & Rees, M. J. 1997, ApJ, 482, L29

Meyer, B. S. 1989, ApJ, 343, 254

Nakamura, T., & Oohara, K. 1991, Prog. Theor. Phys., 86, 73

New, K. C. B., & Tohline, J. E. 1997, ApJ, 490, 311

Oohara, K., & Nakamura, T. 1990, Prog. Theor. Phys., 83, 906

Oohara, K., & Nakamura, T. 1999, Prog. Theor. Phys. Suppl., 136, 270

Paczyński, B. 1991, Acta Astron., 41, 257

Paczyński, B., & Xu, G. 1994, ApJ, 427, 708

Popham, R., Woosley, S. E., & Fryer, C. 1999, ApJ, 518, 356

Qian, Y.-Z., & Woosley, S. E. 1996, ApJ, 471, 331

Rasio, F. A., & Shapiro, S. L. 1992, ApJ, 401, 226

Rasio, F. A., & Shapiro, S. L. 1994, ApJ, 432, 242

Rasio, F. A., & Shapiro, S. L. 1995, ApJ, 438, 887

Rosswog, S., Davies, M. B., Thielemann, F.-K., & Piran, T. 2000, A&A, 360, 171

Rosswog, S., Liebendörfer, M., Thielemann, F.-K., et al. 1999, A&A, 341, 499

Ruffert, M. 1992, A&A, 265, 82

Ruffert, M., & Janka, H.-T. 1998, A&A, 338, 535

Ruffert, M., & Janka, H.-T. 1999, A&A, 344, 573

Ruffert, M., Janka, H.-T., & Schäfer, G. 1996, A&A, 311, 532

Ruffert, M., Janka, H.-T., Takahashi, K., & Schäfer, G. 1997a, A&A, 319, 122

Ruffert, M., Rampp, M., & Janka, H.-T., 1997b, A&A, 321, 991

Sawyer, R. F. 1980, ApJ, 237, 187

Shapiro, S. L., & Teukolsky, S. A. 1983, Black Holes, White Dwarfs, and Neutron Stars (John Wiley & Sons, New York)

Shen, H., Toki, H., Oyamatsu, K., & Sumiyoshi, K. 1998, Nucl. Phys. A, 637, 435

Shibata, M. 1999, Phys. Rev. D, 60, 104052

Shibata, M., & Uryū, K. 2000, Phys. Rev. D, 61, 064001

Shibata, M., & Uryū, K. 2001, in Proc. 20th Texas Symposium on Relativistic Astrophysics and Cosmology, ed. H. Martel, & J. C. Wheeler, in press [astro-ph/0104409]

Shibata, M., Baumgarte, T. W., & Shapiro, S. L. 1998, Phys. Rev. D, 58, 023002

Shibata, M., Baumgarte, T. W., & Shapiro, S. L. 2000, Phys. Rev. D, 61, 044012

Sumiyoshi, K., Yamada, S., Suzuki, H., & Hillebrandt, W. 1998, A&A, 334, 159

Swesty, F. D., Wang, E. Y. M., & Calder, A. C. 2000, ApJ, 541, 937

Symbalisty, E., & Schramm, D. N. 1982, Astrophys. Lett., 22, 143

Taniguchi, K., & Nakamura, T. 1996, Prog. Theor. Phys., 96, 693

Thorne, K. S. 1974, ApJ, 191, 507

Thorne, K. S. 1995, in Procs. of the Snowmass 95 Summer Study on Particle and Nuclear Astrophysics and Cosmology, ed. E. W. Kolb, & R. Peccei (World Scientific, Singapore) 398

Thorne, K. S. 1998, Phys. Rev. D, 58, 124031

Tscharnuter, W. M., & Winkler, K.-H. 1979, Comp. Phys. Comm., 18, 171

van den Horn, L. J., & van Weert, C. G. 1981, Phys. Lett., 84A, 226

Waxman, E., & Bahcall, J. N. 1997, Phys. Rev. Lett., 78, 2292

Waxman, E., & Bahcall, J. N. 2000, ApJ, 541, 707

Weber, F. 1999, Pulsars as Astrophysical Laboratories for Nuclear and Particle Physics (IOP, Bristol)

Woosley, S. E. 1993a, ApJ, 405, 273

Woosley, S. E. 1993b, A&AS, 97, 205

Zhuge, X., Centrella, J. M., & McMillan, S. L. W. 1994, Phys. Rev. D, 50, 6247

Zhuge, X., Centrella, J. M., & McMillan S. L. W. 1996, Phys. Rev. D, 54, 7261